Politecnico di Torino

Ingegneria Biomedica
A.a. 2020/2021
Sessione di Laurea Dicembre 2021

# Development and validation of patient-specific finite element models of metastatic human spine segments

Relatrice:
Prof.ssa Cristina Bignardi
Correlatori:
Prof. Alberto Audenino
Prof. Marco Viceconti
Ing. Cristina Curreli

Candidata:
Elda Paoli

# Abstract

Cancer is one of the major causes of morbidity and mortality in the world and one possible complication is the spread of metastases in the spine. The presence of vertebral metastases strongly affects the anatomical structure and mechanical properties of the bone and can lead to fracture, pain, disability and impairment of quality of life. Evaluating the mechanical strength of the pathologic vertebrae is thus fundamental in order to provide an objective support to the clinic decision and treatment plan. The current clinical methods used for the diagnosis of vertebral fracture are mainly based on bone mineral density and qualitative assessment of radiological data; however, they do not provide an objective and accurate fracture risk estimation. In the last decades, numerical methods have been widely used for decision making in clinical care. In particular, Finite Element (FE) models represent a useful and promising tool to simulate biological tissue behaviour and investigate the effect of critical loading conditions which cannot be tested experimentally. Patient-specific FE models, that include information about the geometry and mechanical properties of the bone, can be developed starting from medical images acquired through non-destructive and non-invasive imaging techniques. Different studies investigated the possibility to use FE analyses to predict vertebral strength and FE models that consider at least two functional spinal units proved to better predict the mechanical response in vivo because the load is physiologically distributed between all vertebrae and intervertebral discs. In the literature there are several FE models of spine segments, developed with different techniques and modelling parameters, but only few studies focused on the validation aspects. One of the possible ways to validate FE models is through Digital Image Correlation (DIC), which is a non-contact optical technique that provides full-field displacement and strain distribution over the specimen surface during the experimental tests.

The aim of this thesis is to develop patient-specific FE models of the spine segments and validate them comparing the surface displacements of vertebral bodies predicted by the models with those measured experimentally using the DIC technique. A validation protocol, recently developed by the In Silico Medicine research group at the Medical Technology Lab - Rizzoli Orthopaedic Institute and at the Industrial Engineering Department - University of Bologna, was studied and applied to two different case studies. In particular, patient-specific FE models of cadaveric thoracolumbar spine segments were first developed starting from CT data; after registration, loading conditions were then defined to simulate the experimental testing; a point-to-point surface

displacement comparison was finally performed. Also, important verification studies were conducted on the definition and implementation of the boundary conditions, repeatability of the experimental measurements and mesh converge analysis. The results obtained in this work allowed to demonstrate the possibility to apply the developed methodology to different case studies and highlight strength and weakness of the validation pipeline.

# Contents

# 1. The spine

The spine, also known as vertebral column, spinal column or rachis, is a very complex structure, situated in the back of the neck and the trunk, and it performs different functions [1]:

- Support of head and trunk in static and dynamic conditions,
- Protection of the spinal cord and nerves.

The spine, in fact, supports head, protects the spinal cord ensuring the exit of the spinal nerves, is a fundamental axis in the complex movements of the trunk and participates in the expansion of the ribs in the respiratory dynamics. Furthermore, it provides attachments for muscles and is also an important site of haemopoiesis throughout life [2].

## 1.1 Anatomy of the spine

The anatomical structure of the spine consists of several mobile elements, connected by numerous fibro-ligamentous elements, which give it a considerable mechanical strength [1]. The spine consists of $33 - 34$ vertebrae, which form the structural bone unit. The vertebral column can be subdivided into five parts in cranio-caudal way:

- Cervical region, consisting of $7$ vertebrae.
- Thoracic or dorsal region, consisting of $12$ vertebrae.
- Lumbar region, consisting of $5$ vertebrae.
- Sacral region, consisting of $5$ vertebrae fused together in the sacrum.
- Coccygeal region, consisting in $4$ vertebrae fused together in the coccyx.

The vertebrae are considered as short and irregular bones, consisting mainly of cancellous or trabecular bone, coated with a thin layer of cortical bone. These two types of bone have different porosity ($5 - 15\%$ for the cortical bone, $40 - 95\%$ for the trabecular bone [3]), that means different mechanical behaviour and properties.

The cortical bone can be treated as anisotropic: the mechanical properties, such as the strength, are greater along the longitudinal direction than those along the radial and circumferential direction. Since some studies show comparatively small differences in these properties in the last two direction, cortical bone can be considered as a transversely isotropic material [3].

The trabecular bone is a highly porous material with anisotropic mechanical properties. As for the cortical bone, the strength of trabecular bone is greater in compression than tension. Despite the trabecular bone yields at strains of approximately $0.7\%$ in compression, it can support compressive strains of up to $50\%$ while preserving a large part of its load-bearing capacity [3]. Cancellous bone shows substantial spatial heterogeneity in density and trabecular architecture and these variations can lead to heterogeneity in elastic and strength properties [3].

As shown in figure 1.1, the vertebrae consist of an anterior body and a posterior neural arch, that delimit the foramen, an opening which encloses and protects the spinal cord, meninges and their vessels. The vertebral body presents a thin cortical shell surrounding a network of trabecular bone [4]. The vertebral arch is composed of two anterior, bilateral and short portions, the pedicles, which are torn by the vertebral body, followed by two wider posterior plate-like portions, the laminae. From the junction of pedicles and laminae a series of processes comes from: a transverse process and two articular processes, superior and inferior, on each side of the vertebra. Furthermore, the spinous process comes from the posterior union of the laminae [1]. Each element of a vertebra has a major functional role. The vertebral body has the weight-bearing function, the articular processes determine the direction of motion and restrict abnormal movement, the vertebral arch encloses the spinal cord and the spinous and transverse processes serve as bony levers for muscle and ligament attachment [5].

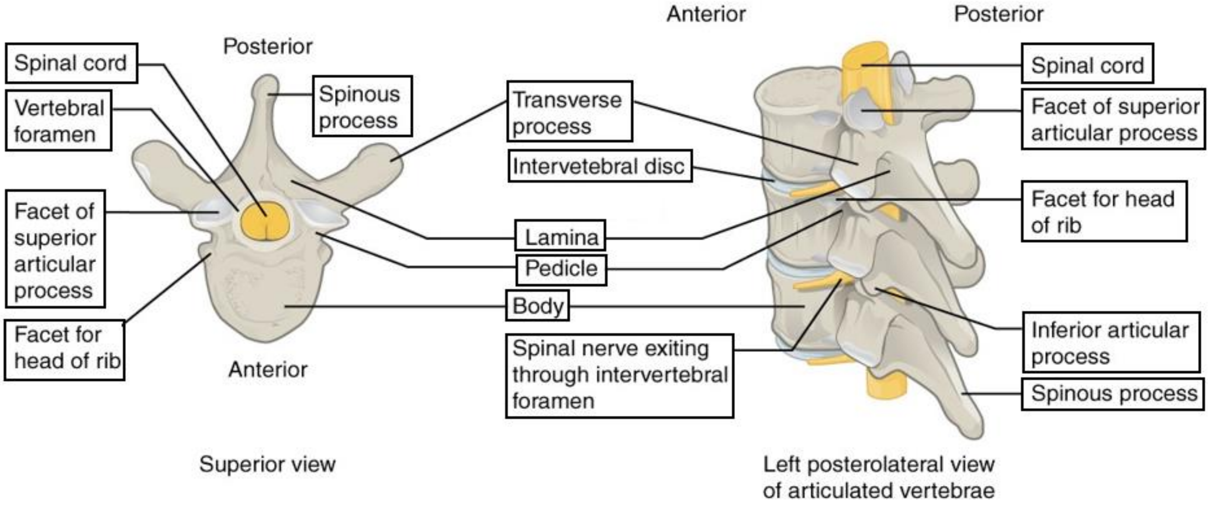

*Figure 1.1: Anatomy of the vertebrae.*

The morphological characteristics, such as size, shape and proportions, of the vertebrae change depending to the different region in which they are found. The dimensions of the vertebral bodies, for example, increase in the cranio-caudal direction up to the fourth lumbar vertebra due to increased weight and pressure that they must sustain, then the width decreases gradually up to the apex of the coccyx. The vertebrae are articulated by the interposition of complex structures, the intervertebral discs (IVDs), which are fibrocartilaginous pads, whose mechanical properties vary considerably with age and degeneration [6]. As shown in figure 1.2, the intervertebral disc has three main components:

- The nucleus pulposus (NP) is a soft, deformable and gelatinous structure. Its main constituents are proteoglycans, type II collagen (only $5\%$ of the mass of the nucleus [7]) and water. The nucleus pulposus exhibits fluid-like mechanical properties at low loading rates, while it behaves more solid-like at high loading rate [8]. The function of the nucleus is to respond to the stresses acting on the column and to distribute them evenly to the annulus: in fact, thanks to its composition, the pressure exerted on the disc is transmitted radially.
- The annulus fibrosus (AF) surrounded the nucleus pulposus and is composed of oriented type I collagen, proteoglycans and water. In contrast to the nucleus pulposus, the annulus has high collagen to proteoglycan ratio, making it a more rigid structure with high tensile strength [4]. The annulus fibrosus is made up of $15-25$ concentric and densely packed layers, the lamellae, which are approximately $0.05-0.5\,mm$ thick [6]. Each layer consists of strong collagen fibre bundles, which alternate their orientation between $\pm25-45°$ [6]. Thanks to the arrangement of the fibre bundles, the annulus has considerable strength.
- The endplates are thin bilayers of relatively tough hyaline cartilage and cortical bone that separate the intervertebral disks from the vertebral body above and below. Their presence attempts to prevents the nucleus herniation in the adjacent vertebral bodies.

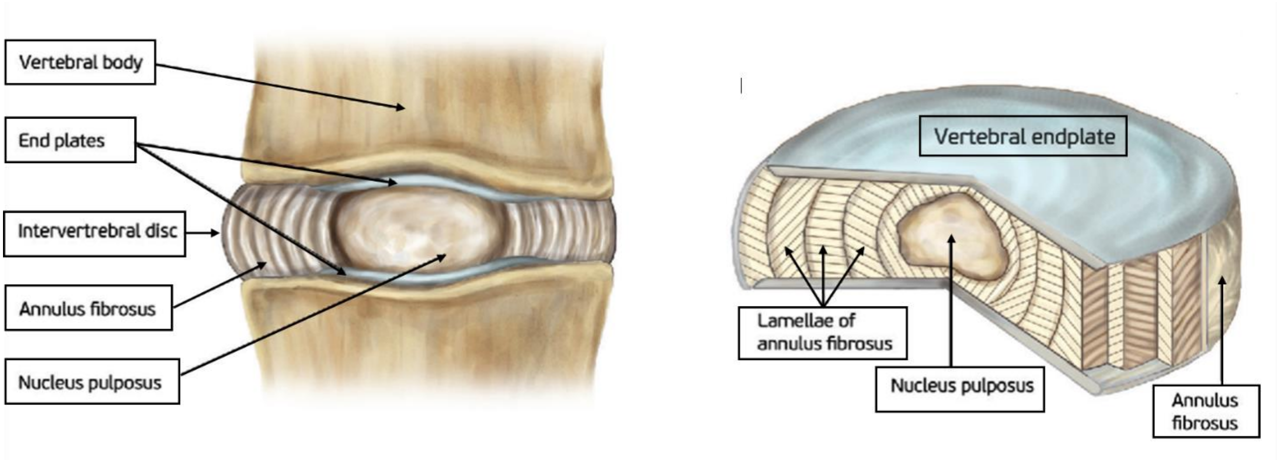

*Figure 1.2: Anatomy of an intervertebral disc.*

The thickness of the intervertebral discs increases in cranio-caudal way. Furthermore, the size and shape of intervertebral discs vary with spinal level giving rise to systematic changes in intradiscal stresses: for example, after normalisation for size, cervical segments are stronger in compression than lumbar ones, but weaker in bending [6]. The intervertebral discs allow the vertebral column to twist and bend, absorb the mechanical stresses sustained by the spine and distribute compressive loading on the adjacent vertebral bodies. The ability of the intervertebral disc to support axial compression is due to its composition, in particular to its internal pressure resulting from the attraction of water by its proteoglycans [7]. The relative compositions of the nucleus and annulus suggest that the nucleus can support a higher proportion of the compressive load than the annulus. When the intervertebral disc is subjected to compression loads, the height of the nucleus is reduced and it tries to expand towards the collagen rings of the annulus. The mechanical role of the fibres of the annulus is to balance the radial pressure exerted by the nucleus on the annulus: in fact, when the nucleus pushes on the annulus, the fibres stretch quickly and develop elastic tension. Furthermore, as the nucleus is also constrained longitudinally by the endplates and the vertebral bodies, the pressure applied to it is passed on to both the annulus and the endplates and thus the load is transmitted from one vertebra to the other. After the removal of the load, the normal shape of the nucleus is restored because the elastic energy stored in the collagen rings allows the recoil of the annulus. The facet joints also deformed, as do the ligaments, tendons and muscles; in this way the compression loads are shared by several structures and no single tissue risks injury. The spine, observed in the frontal plane, is rectilinear, while, if observed in the sagittal plane, it has some anatomical curvatures (Fig. 1.3): two with anterior concavity, thoracic and sacral kyphosis, and two with anterior convexity, cervical and lumbar lordosis.

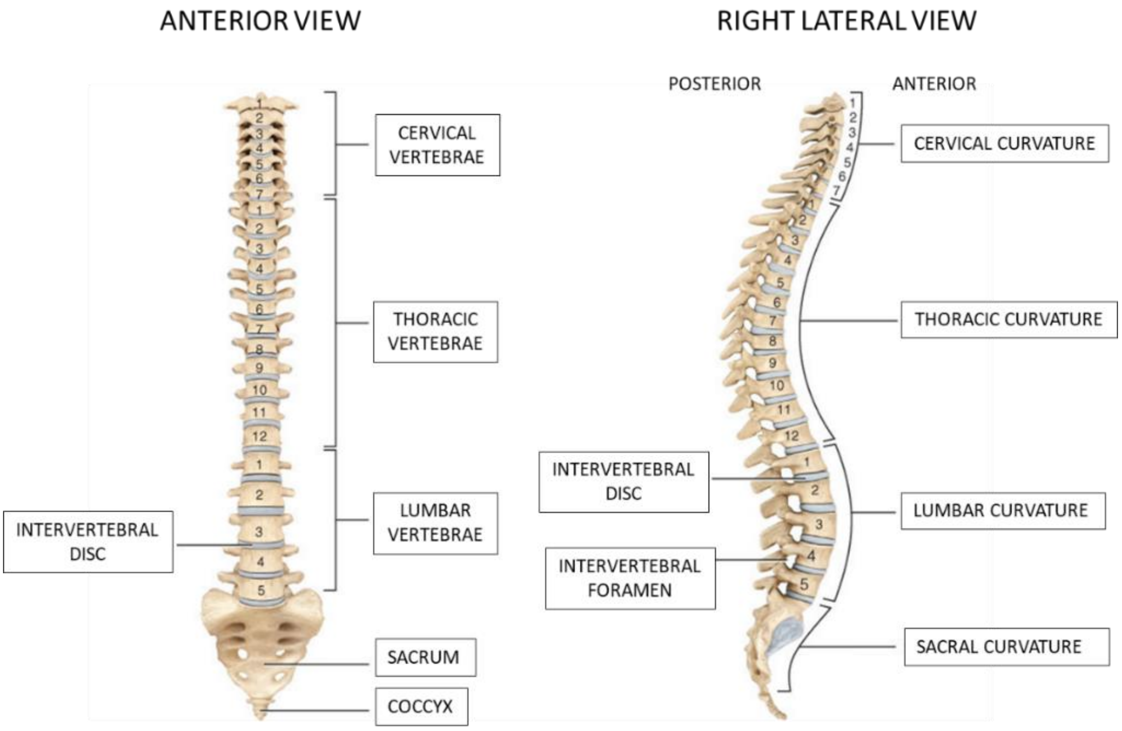
ANTERIOR VIEW

RIGHT LATERAL VIEW

*Figure 1.3: Physiological curvatures of the spine.*

The functional spinal unit (FSU) is the basic building block of the spine and consists of two adjacent vertebrae and the intervertebral disc, the facet joints and the spinal ligaments between them (Fig. 1.4).

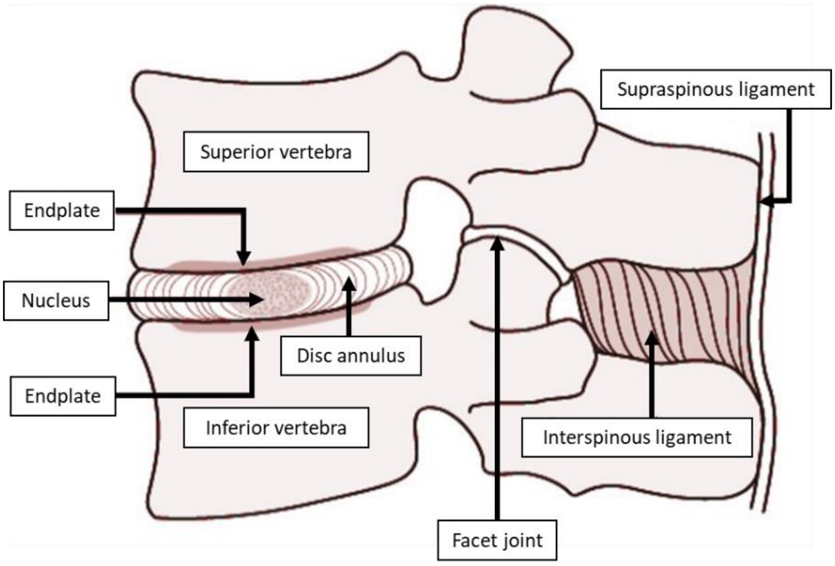

*Figure 1.4: A functional spinal unit.*

The structures of the FSU are coordinated anatomically and functionally: a lesion on one of its components also influences the other parts. The FSU can be divided into two parts:

- The anterior pillar, consisting of the stacked vertebral bodies and the intervertebral disc, with supporting function: it absorbs and transfers the axial compression loads, such as the body weight.
- The posterior pillar, consisting of the joints of the vertebral arch, with dynamic function: it allows the movements permitted by the shape of the joints and prevents those limited by the ligament structures, the joint position and the annulus fibrosus.

These pillars progressively increase in size from the cervical to the lumbar vertebrae as a mechanical adaptation to increasingly progressive load to which the vertebrae are subjected in the erect position.

## 1.2 Biomechanics of the spine

The biomechanical function of the vertebral column is to provide structural support, enable trunk movements and protect the neural elements. The succession of vertebrae and intervertebral discs forms the rigid, but at the same time flexible, central axis of the body and supports the full weight of the head and trunk. It also transmits even greater forces generated by muscle attached to it directly or indirectly. The spine is subjected to stress and strain in daily activities, such as sitting, walking, and even lying down. During these activities, the rachis undergoes:

- Compressive forces, absorbed mainly by the anterior part of the column.
- Torsion forces, which mostly act on the posterior joints.
- Shear and tensile forces, generated mainly by movements of flexion and extension.

The spine, normally subject to compression caused by the upper body weight, is designed to resist to significant forces without crushing: each vertebral body and each intervertebral disc, placed one above the other, tend to deform shortening along the direction of force and expanding laterally [9]. The human spine needs to be kept mechanically stable during movements and this is the role of the complex neuromuscular system. The stability of the spine depends on several factors, but essentially it is maintained by the relationship of the gravity line with the vertebral segments [5]. The movement between vertebrae takes place essentially at the fibrocartilaginous intervertebral discs and at the joints formed by the inferior facets of the superior vertebra and the superior facets of the inferior vertebra. The vertebral body can move in the sagittal, frontal and transverse planes and also rotate around the three same axes: each body, therefore, has six degrees of movement. Although the vertebrae may partly move in all directions, the magnitude of such movements varies in the different spinal level. Physiological movement of a vertebral segment relative to its supporting structure during daily activities is complex because it involves a combination of plane movements: lateral flexion on the coronal plane, rotation on the transverse plane, antero-flexion and retro-extension on the sagittal plane (Fig 1.5).

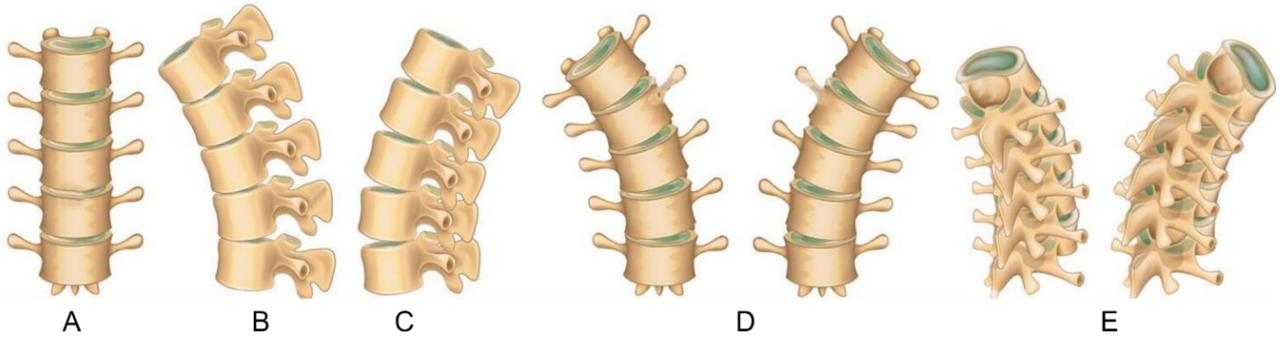

*Figure 1.5: Physiological movements of spine. A: Neutral position; B: Antero-flexion; C: Retro-extension; D: Lateral flexion; E: Rotation.*

While normal motion of any one vertebra is quite minimal, the cumulative effect of the movement of the 24 movable vertebrae is considerable. In fact, the flexibility of the vertebral column is obtained through small movements of several elements which constitute it. The advantage of this configuration is that for the achievement of a wide and complete mobility, small movements of the single functional spinal unit are sufficient. The existence of numerous segments relatively immovable generates a situation more stable that the one provided by a few very mobile joints. Normal mobility of the spinal column varies considerably and it may be influenced by age, sex, ligamentous laxity, congenital factors and pathology [10]. Other factors that influence the spinal segment motion include the thickness of intervertebral disc, the compliance of its fibrocartilage, the shape and orientation of the articular processes and the dimensions and shape of the adjacent vertebral endplates. The basic movements of the vertebral column are:

- Flexion (forward bending) in the sagittal plane, which is the most pronounced spinal motion. About 75% of all spinal flexion below the neck occurs in the lumbar spine and about 70% of all lumbar flexion occurs at the lumbosacral joint [5]. During flexion, the anterior edges of the vertebrae get close, while the posterior ones separate. The anterior part of the intervertebral disc is compressed, tending to push the nucleus pulposus posteriorly. The principal limiting factor to movement is tension in postvertebral muscles. In flexion, compressive loading on the spine is applied asymmetrically to the vertebral bodies by the intervertebral disc and is variably shared between the disc and apophyseal joints [11]. Since high compressive loading of the human spine usually occurs in flexed postures, the anterior wedge fracture is the most frequent type of osteoporotic vertebral fracture [11].
- Extension (backward bending) in the sagittal plane, which has a much lower magnitude than flexion. In this case, the posterior edges of the vertebrae approach and the anterior ones separate. The posterior part of the intervertebral disc is compressed and the motion is adjusted by the anterior annulus of the disc, the anterior longitudinal ligament, all the anterior and lateral muscles which contribute to flexion, the anterior fascia and visceral attachments. While flexed postures result in more vertebral body loading, extended postures create more neural arch loading [8].
- Rotation, which is limited by the geometry of the articular facets, the thickness of the discs and the resistance offered by the fibres of the disc's annulus and the vertebral ligaments.

Although part of the axial load is supported by the vertebral facets, the majority of compression load is sustained by the vertebral bodies, whose strength in axial compression increases along the entire spinal column from cervical to lumbar region due largely to increasing cross-sectional area [8]. The load upon the superior endplate is directed to the inferior endplate via the cancellous core and the cortical shell of each vertebra. The trabecular core not only shares load distribution with the cortical shell, but during loading, especially at high rates, it serves as the main resistor of dynamic peak loads via its trabeculae and marrow, which absorb energy [5]. In fact, the trabecular core can undergo up to $9.5\%$ deformation prior to fracture, as compared to only $2\%$ for the cortical shell [5]. Bone strength seems to be directly related to mineral content and a small loss of osseous tissue has a large effect on bone strength: a $25\%$ loss of osseous tissue results in a reduction of bone strength of about $50\%$ [5].

The physiological spinal curves offer the vertebral column increased flexibility, elasticity, strength to axial compression stresses and shock-absorbing capability while still maintaining an adequate degree of stiffness and stability between vertebral segments. The human spine, like any other biological system, can be studied from the biomechanics point of view, analysing its structure, function and motion. In particular, the biomechanics of the spine is often investigated through experimental studies. Biomechanical tests usually involve only a functional spinal unit, but sometimes large specimens, comprising three or more vertebrae, are tested. An FSU can be tested loading to failure in order to evaluate its strength or applying sub-failure loads in order to simulate physiological condition. Despite the two approaches are different, both are useful to characterise different aspects of the biomechanical behaviour. Since spinal joints are subjected to complex three-dimensional loading in vivo, over the years the mechanical response of the FSUs under uniaxial compression, axial rotation, lateral bending and flexion/extension was studied: generally, strength is greatest in axial rotation, followed by extension, lateral bending, and finally flexion [6].

## 1.3 Pathology of the spine

The pathologies which affect the spine can be degenerative, traumatic, infectious or tumour-related and can involve bone, joints, ligament structures and also the nerve structures (nerve roots and/or spinal cord). One of the most common injuries of the spine is the compression fracture of the vertebral body and these fractures are related to various pathologies, such as osteoporosis and metastases [9]; this work focuses particularly on the latter.

### 1.3.1 Vertebral metastases

Cancer is one of the major causes of morbidity and mortality across the world: every day in Italy more than 1,000 new cases of cancer are diagnosed. It is estimated, in fact, that in our Country there were about 377,000 new diagnoses of cancer in 2020 [12]. Any cancer can spread to bone, but in adults more than 75% of skeletal metastases originate from cancers of the prostate, breast, kidney and lung [2]. The metastases may occur in any bone, but most involve the axial skeleton, proximal femur and humerus, where the red marrow, with its rich capillary network and slow blood flow, facilitates implantation and growth of the tumour cells [2]. In particular, the spine is one of the most frequent sites for bone metastases (over $70\%$ of metastases are located here [13]) and the metastatic lesions mainly involve the vertebral body ($80\%$ of spinal metastases [14]) rather than the posterior elements. Due to the vertebral body size, the metastases occur most frequently in the lumbar vertebrae, followed by the thoracic and then the cervical ones. The metastases can be of three different types (Fig $1.6$) depending on how they interfere with the normal bone remodelling:

- Lytic lesions, characterized by the rarefaction of the bone network, the degradation of the trabecular bone microarchitecture, the creation of focal bone loss (cavities) and the destruction of a significant portion of the cortex. They represent 95% of the spinal metastases developed at advanced stage of cancer [15]. The metastatic cells do not directly resorb bone, but they secrete substances that stimulate osteoclastic bone resorption [2]. In fact, lytic lesions appear in radiological images as regions with very low volumetric bone mineral density (BMD) and produce a decrease in bone strength and an increase in bone fragility and risk of fracture [13]. The osteolytic vertebrae exhibit the lowest bone volume fraction BV/TV, that is the volume of mineralised bone per unit volume of the sample, of the three lesion groups [16].
- Blastic lesions consist in the irregular formation of immature and poor-quality bone. The osteoblastic vertebrae were characterized by an overall increased bone density and exhibit higher median BV/TV values ($+53\%$) compared to vertebrae with mixed or osteolytic lesions [16]. In this case trabeculae appear abnormally thick and interconnected, sometimes without clear preferred orientation. Although the increase in bone volume and osteoid deposition, the bone is of inferior quality and the lower intrinsic properties can be explained with the high amount of new, less mineralized tissue and unorganized collagen structure. However, blastic vertebrae were significantly stronger than the lytic and mixed ones ($+700\%$ in strength) [16]. The increased strength of osteoblastic vertebrae is predominantly due to densification of the bone architecture (higher BV/TV and higher bone mineral content values) despite lower tissue properties [16].
- Mixed lesions, which present both lytic and blastic phenotypes.

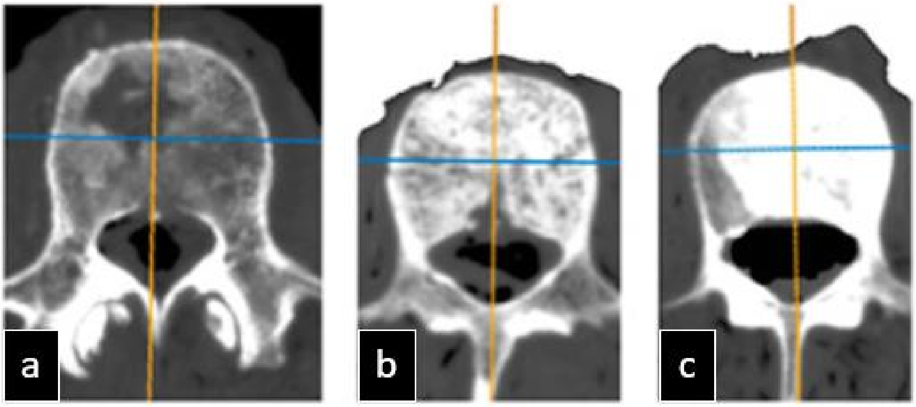

*Figure 1.6: Types of bone metastases. A: Lytic; B: Mixed; C: Blastic.*

The metastatic type influences the mechanical behaviour of the vertebrae. In particular, the vertebrae with lytic metastases show more critical deformation, while the vertebrae with mixed or blastic metastases deform similarly or less than the healthy ones [17]. The presence of vertebral metastases strongly affects the anatomical structure and mechanical properties of the bone and may lead to spine instability and increase the risk of fractures. The possible treatments for metastatic spinal disease are medical therapy, surgery and radiation. To choose the most suitable treatment the clinicians should consider the neurological status, the general health, the age and the anatomical extent of disease of the patient. The total resection surgery was considered for years the most appropriate initial therapy, but such an invasive approach is not feasible in most patients [14]. Therefore, currently the radiation therapy (radiotherapy and chemotherapy) is the most common treatment, while the surgery is reserved for neurological compromise, radiation failure, spinal instability or uncertain diagnosis [14].

### 1.3.2 Vertebral fractures

The vertebral fractures can occur after the application of a single abnormal and traumatic load, that overcome the mechanical strength of the bone, or after the application of physiological loads when the bone structure is weakened and damaged. The biological materials can change their properties in normal physiological conditions (for example, bone remodelling) or in pathological conditions. These conditions can also affect the mechanical properties, such as the rigidity and strength. This thesis will be focused on pathological vertebral fractures of cancer patients with metastatic spine disease: these fractures are a direct consequence of the effect of bone metastases on the anatomy and structure of vertebral bone. Pathological vertebral fractures are an integral part of spinal adverse events and occur in $15-20\%$ of patients with spinal bone metastases and, once fractured, further collapse of the vertebral body may cause loss of vertebral height, kyphoscoliosis and restrictive lung disease [16]. Vertebral fractures cause pain, disability, neurological deficit, severe impairment of quality of life and are directly associated with significant shortening of patient's survival [16], [18]. Despite the clear clinical importance of vertebral fractures, they remain underdiagnosed in clinical practice because the radiologic evidence of metastases does not become apparent on plain radiographs until approximately $30\%$ to $50\%$ of the bone is destroyed and because the typical symptoms, such as back pain and restricted movement, are mild and nonspecific and are usually attributed to degenerative change [19]. Vertebral fractures, like fractures in the peripheral skeleton, occur in a predictable and reproducible manner and, consequently, can be classified in order to facilitate communication between clinicians of the spine community and encourage optimal treatment protocols. Fractures of vertebral column are divided traditionally into those affecting the thoracolumbar and the cervical region. Because the fracture pattern and the mechanism share many similarities, some classification schemes have been proposed for cervical and thoracolumbar fractures over the years. Since only specimen with thoracic and lumbar vertebrae have been analysed for this thesis, only the more commonly used classification of thoracolumbar injuries, called AOSpine classification, is presented below. This classification is based primarily in the pathomorphological characteristics of the injuries and the three main categories (type A, B and C), have typical fundamental injury patterns, which are defined by a few radiological criteria that are easily recognizable [20] [21]. Each main type can be further classified based on morphological criteria into distinct groups (1, 2, 3) and each group, in its turn, into subgroups (.1, .2, .3.). Focusing only on the main groups, they are (Fig. 1.7):

- Type A: compression injuries (vertebral body compression injuries).

  These injuries are caused by axial compression and affect almost exclusively the anterior elements of the vertebral column (vertebral body and/or intervertebral disc). The height of the vertebral body is reduced and a shortening of the anterior column occurs. The posterior ligamentous complex is intact.
- Type B: distraction injuries (anterior and posterior element injuries with distraction).

  These injuries are characterized by a transverse disruption with elongation of the distance between posterior or anterior vertebral elements. The degree of instability ranges from partial to complete and the frequency of neurological impairment is significantly higher than in type A injuries.

- Type C: translation injuries (anterior and posterior element injuries with rotation).

  These rotational injuries focus on injury patterns resulting from axial torque. Since the complete separation of the vertebral elements can occur without any remaining intact anterior or posterior structure, rotational fractures represent the severest injuries of the thoracolumbar spine and are associated with the highest rate of neurological deficit. Some of the common characteristics are rotational displacement, disruption of all longitudinal ligaments and of the disc, fractures of all articular and transverse processes and asymmetrical fractures of the vertebral body.

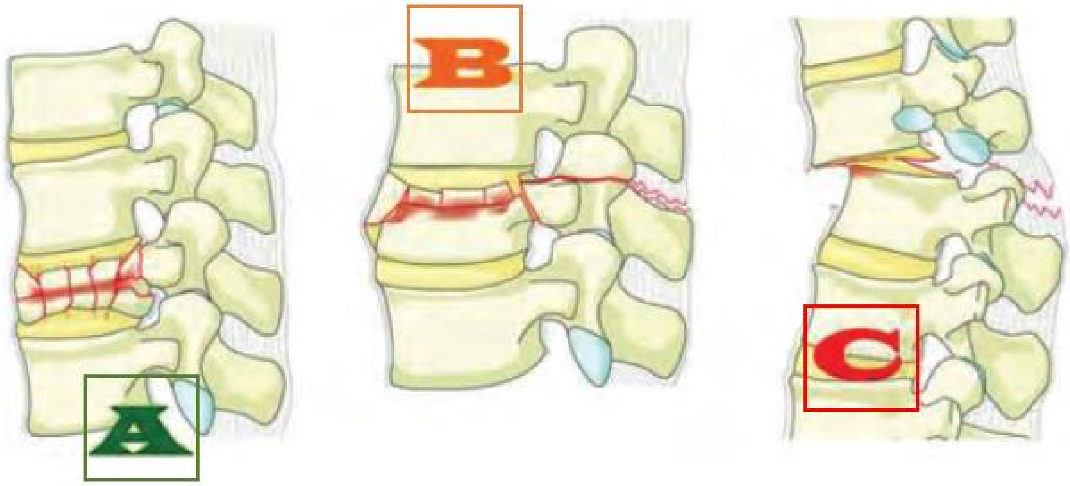

*Figure 1.7: Types of vertebral fractures. A: Compression injury; B: Distraction injury; C: Translation injury*

The alteration of the anatomical composition of the bone in the vertebral body results in a decrease in its load-bearing capacity of the spine. The load-bearing capacity depends on several factors, including the area and the bone mineral density of the intact body and the metastatic lesion size [19]. Bone strength is a function of geometry, material properties and loading conditions. Since metastatic lesions can affect the geometry and material properties of bones, the strength of the bone can also be affected. The stability of the spinal column and the risk of vertebral fracture are very difficult to quantify. The current clinical methods used to evaluate the pathological risk of fracture are mainly based on bone mineral density (BMD), measured with dual X-ray absorptiometry (DXA), and qualitative assessments of radiological data. These methods, however, are not enough to provide an objective and accurate prediction of bone strength. Several clinical factors are associated with the risk of fracture, which therefore cannot be assessed only on the basis of bone mineral density. The Fracture Risk Assessment Tool (FRAX) considers several clinical risk factors, such as age, vertebral height, bone mineral density, to predict fractures. Specifically for patients with spinal metastases, there is a scoring system, called Spinal Instability Neoplastic Score (SINS), developed to help clinicians to assess critical metastases, estimate the overall spine stability and predict the risk of vertebral fracture in order to prescribe the appropriate treatment for the patients. This score is calculated considering five objective radiographic criteria (location of the metastatic vertebra, bone lesion type, spinal alignment, vertebral body collapse and posterolateral structures involvement) and a subjective patient symptom (the pain) [17]. These are the possible outcomes:

- Score 0-6: stable
- Score 7-12: potentially unstable
- Score 13-18: unstable

A SINS of 7-12 is uncertain because there are not clear guidelines and the decision is left to the experience of the clinicians. A limitation of the SINS system is that it does not account for the effect of the features of the lesion, as its size and location, over vertebral stability. This scoring system, therefore, lacks specificity and provides uncertain indications over a wide range of cases.

# 2. Finite Element modelling of the spine

In this chapter the mathematical theory behind the Finite Element Method will be explained. Later, the potential and the advantages of the application of FEM in biomechanics will be presented, focusing on the development of patient-specific finite element (FE) models. Therefore, a state-of-art review about the FE models of the spine segments and the possible modelling techniques will be exposed. Finally, the aspect of the validation of the FE models will be analysed and one possible way to perform the validation will be mentioned.

## 2.1 The Finite Element Method

The equations governing real physical phenomena, such as deformations in solid continuum mechanics problems, are generally partial differential equations (PDEs), usually nonlinear, which are extremely difficult to solve analytically. Only in some simple cases it is possible to obtain an analytic solution of the equations by applying, for example, the methods based on Fourier and Laplace Transform [22]. For more complex problems, for instance when modelling three-dimensional bodies such as bones, it is necessary to introduce hypothesis and idealizations to make the problem mathematically easier. The link between the real physical system and the analytic solution is provided by the mathematical model of the system, which is defined by equations usually solved by applying powerful numerical methods [22], including the Finite Element Method.

The Finite Element Method (FEM) is an extremely powerful and versatile tool widely used in engineering analyses to solve physical problems. FEM is a numerical technique used to solve problems described by partial differential equations and provides an approximate numerical solution. The basic concept is the discretization of the continuous model: the domain of interest is represented as an assembly of finite elements of elementary geometric shape connected to each other through nodes. It is fundamental that the subdivision into elements respects the constrain of conformity between contiguous elements: two contiguous 2D elements must share one edge, while two contiguous 3D elements one face. Differential equations which describe the physical problem, instead, are left unchanged. Through discretization, the continuous problem, which initially has an infinite number of unknows, consisting of the values of the continuous function at each point of the domain of interest, is reduced to a problem with a finite number of unknows, that are the values assumed by the variables in some specific points of the domain, the nodes. Nodal values define uniquely the trend of the variable within the element through know approximate functions, also called shape functions, which are generally polynomial [22]. Each continuous function, in fact, can be approximated by a sufficiently high polynomial degree. The order of the polynomial used to approximate the actual solution affects the accuracy with which the solution of the differential equations can be evaluated: the higher the degree, the better the approximation [22]. The accuracy of the approximation depends not only on the degree of the polynomial, but also on the size of the subdivision interval [22]. In case of strong gradients of the function to be approximated, one possible strategy to obtain better results is the thickening of the mesh, that is the increase of the density of the elements. The thickening does not necessarily have to be uniform, but it is appropriate that it is applied only where it is necessary: it is called, therefore, selective thickening. This possibility is one of the major advantages of FEM.

A continuous physical problem can be thus transformed into a discretized finite element problem with unknown nodal values, which, once known, allow to establish the values inside the elements through the shape functions.

The figure 2.1 shows the basic principle of the FEM in the one-dimensional case: after the subdivision of the integration domain into intervals, the unknow function $u(x)$ is approximated with a function with known trend $\bar{u}(x)$. To do this, it is sufficient to determine the approximated values $\bar{u}_h$ of the unknown function in the nodes, from which the values between the nodes can be easily interpolated [23].

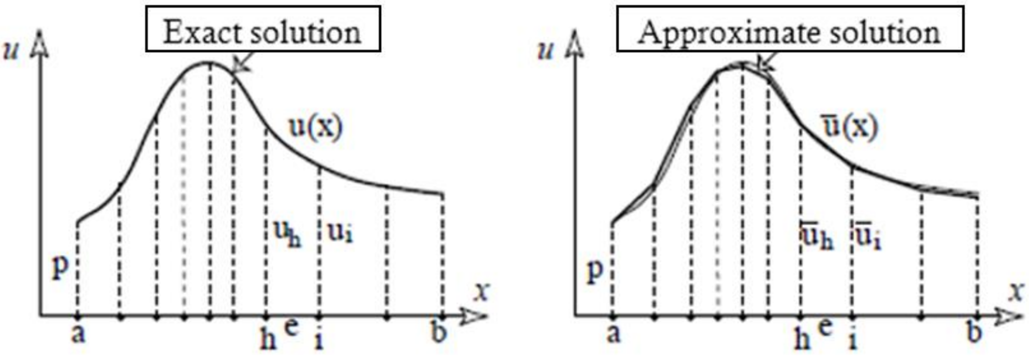

Figure 2.1: Discretization in one-dimension.

## 2.2 Patient-specific Finite Element models

Finite Element modelling for biomechanical analysis, in which there are complex geometries and boundary conditions, represents a useful and promising tool in decision making and optimizing individual therapy. In biomechanics the FEM allows to simulate the biological tissue behaviour, analyse critical loading conditions which are not feasible to test experimentally, compute non-invasively the stress and strain distribution and determine the bone strength. While in other field of engineering the geometry of the bodies can be easily designed, in biomechanics it is usually reconstructed starting from medical images due to their complexity and variability. This allows to obtain patient-specific FE models, which are of fundamental importance in clinical practice because the geometry and the mechanical properties of every bone are unique and cannot be easily generalized. In particular, the geometry of patient-specific models is acquired through non-destructive and non-invasive medical imaging techniques, such as the computed tomography (CT), which constitutes the most reliable source of information about the morphology and the mechanical properties of the skeletal segments of living patients. CT exploits the interaction between an X-ray beam and the biological tissues through which it passes. Over the years, also high-resolution imaging techniques based on CT have been developed, such as the micro-computed tomography (microCT) and the quantitative computed tomography (QCT).

The microCT imaging can accurately resolve bone morphology and heterogeneities in detail. Resolving bone microstructure, micro-computed tomography based finite elements (microFE) models have become a popular tool for non-destructive structural analysis of cancellous bone tissue and can provide a more detailed understanding about the effect of diseases on the local and structural properties of bones.

The QCT is a well-established technique for the measurement of the bone mineral density in the spine and peripheral skeleton. In particular, since the high responsiveness of spinal cancellous bone and its importance for vertebral strength, QCT is principally used to determine trabecular BMD in the vertebral body and, consequently, to predict vertebral fractures [24]. The spinal QCT examination, performed on standard clinical CT scanners, gives lower radiation exposure than standard CT [24].

Finally, there is also the magnetic resonance imaging (MRI), based on strong magnetic fields, which is suitable to analysed hydrated structures and soft tissues, such as tendons, cartilage and intervertebral discs.

### 2.2.1 Finite Element models of the spine

Patient-specific FE models of spine segments are proposed as a tool to help researchers understanding the relationship between vertebral loading and fractures and to improve fracture risk assessment. FE models of isolated vertebrae cannot accurately predict the vertebral strength because the load is physiologically distributed between vertebral body, posterior elements and intervertebral discs. For this reason, patient-specific FE models of at least a functional spinal unit should be developed and validated to predict the mechanical response in vivo. The existing literature contains several FE models of spine segments, developed using different techniques and modelling parameters.

Lee et al. [11] proposed a subject-specific FE model of an FSU, developed combining the QCT and MRI images, for estimating the vertebral strength and the fracture risk. Their aim was reproducing the mechanical response of the FSU during forward bending, which represented a critical condition due to the high compressive loading. The vertebrae were modelled as transversely isotropic linear-elastic material, while the intervertebral disc as homogeneous and linear-elastic material. The results showed that vertebral strength values measured experimentally during a mechanical test were significantly ($p < 0.0001$) and highly ($R^2 = 0.80 - 0.87$) correlated with those predicted by the FSU FE model. Furthermore, the results proved that the values obtained by the FE analysis were better strength predictor than ones based on areal BMD measured by DXA ($R^2 = 0.54$) and than ones based on volumetric BMD from CT ($R^2 = 0.79$). This outcome highlighted in particular that the areal BMD is only one of the several factors which influence vertebral strength. Therefore, a subject-specific FE models of a FSU could predict the vertebral strength better than BMD alone.

In the finite element modelling of the spine, an accurate mechanical characterization of the intervertebral disc and a detailed analysis of its properties are required to obtain a realistic behaviour of the model. In fact, regarding the kinematic and structural behaviour of the human spine, the most influential element is the intervertebral disc.

The easiest way to model the intervertebral disc is to consider it as a single material.

Wang and Li [21] considered the IVD a single incompressible material, whose mechanical properties are linear and isotropic. Specifically, they attributed to the disc a Young's modulus of $4\ MPa$ and a Poisson's ratio of $0.44449$.

Alternatively, the intervertebral disc can be modelled more accurately and realistically considering the strongly different mechanical properties of its components.

Lee et al. [11] modelled the IVD with two components, the nucleus pulposus and the annulus fibrosus, and assigned to them homogeneous linear-elastic properties taken from the literature: $E = 500\ MPa$ and $\nu = 0.3$ for AF and $E = 8\ MPa$ and $\nu = 0.499$ for NP.

Also Yoon et al. [26] developed a FE model of healthy human intervertebral disc consisting of NP and AF starting from MRI images. Both materials were considered linear elastic solid and the properties were assigned based on literature: $E = 4.2\ MPa$ and $\nu = 0.45$ for AF and $E = 0.2\ MPa$ and $\nu = 0.49$ for NP. The meshes of the two constituents of the disc were generated with two different element types due to the different values of the Poisson's ratio.

Cappetti et al. [27], using the Shirazi Adl's model, modelled the annulus as a system consisting of three overlapped bands containing eight fibre layers and the nucleus as an incompressible non-viscous fluid. For each part of the model, they used a homogeneous, linear, isotropic and elastic material. In this study they evaluated the influence of the disc's geometrical parameters on its mechanical behaviour using the FEM. The disc has a central effect on the simulated biomechanics of the lumbar spine, but their analysis showed that only few parameters, such as disc height and length, were necessary to explain a large portion of the total variance of the model response.

Argoubi et al. [28] considered the intervertebral disc as composed by four main isotropic-homogeneous materials: the annulus fibrosus, the nucleus pulposus and two cartilaginous endplates. The Poisson's ratio assigned to all the components was $0.1$, while the elastic modulus was, respectively, $2.5\ MPa$, $1.5\ MPa$ and $5\ MPa$.

Gomez et al. [29] developed a FE model of an intervertebral disc with the same previous components, but their modelling was more complex. In particular, they considered the NP a non-linear incompressible and hyper-elastic Mooney-Rivlin solid material. Furthermore, the AF was modelled with five homogeneous layers of oriented fibres. The model was thus totally described by 11 material parameters, which were later optimized in order to correctly describe the behaviour of the human disc FE model.

### 2.2.2 Finite Element models of metastatic vertebrae

It is fundamental to study the effect of the vertebral metastases on the bone structure, the mechanical behaviour, the material properties and the strength.

Costa et al. [15] used microCT based finite elements models (microFE) of human vertebral bodies to analyse the effect of the size and location of virtually simulated lytic lesions on the mechanical behaviour and on the risk of vertebral burst fracture initiation. Bone was modelled as a homogeneous, isotropic and linear elastic material with elastic modulus equal to $12\ GPa$ and Poisson’s ratio equal to $0.3$. Each vertebra was loaded in axial compression. Lytic lesions were simulated as single or multiple spherical holes with different sizes and locations in the vertebral body. Results showed that the size of the lesions was linearly related to a decrease in predicted structural properties, while the number and the location had a minor effect.

In many patients with vertebral metastases the BMD decreases as consequence of hormone manipulation and/or chemotherapy, leading to osteopenia and osteoporosis and increasing the risk of vertebral fracturs [30].

Salvatore et al. [30] analysed the biomechanical effect of a metastatic lesion in a osteoporotic lumbar spine model. In detail, they analysed the effect of metastatic size and bone mineral density on the vertebral bulge (the radial displacement) and the vertebral height (the axial displacement). A parametric analysis was performed varying metastasis size (from $15\%$ to $30\%$ of the vertebral body volume) and BMD (osteoporosis was defined by a $66\%$ reduction in the elastic moduli of all bony structures for the cancellous bone and by a $33\%$ for the cortical shell, the endplates, and the posterior elements, while the soft tissue structures were left unchanged). The results showed that the presence of a metastatic lesion in the osteoporotic spine always increased the risk of vertebral fracture and that the larger the size of the metastasis the higher the risk. Furthermore, their study demonstrated that an increment in metastatic lesion size in the spine with a normal BMD has a greater effect on vertebral stability than to the osteoporotic spine.

## 2.3 Validation of Finite Element models

The validation of FE models, that is the assessment of the quality of the models and their predictive capability is still a big challenge in biomechanics, but it is required before introducing such models in clinical practice. Every modelling method requires a complete verification, validation and uncertainty quantification assessment. The validation is usually done by comparing the results of the numerical simulations with the experimental data. In particular, a model can be considered validated if the numerical value of a specific variable computed in a simulation satisfactorily matches the numerical value from the experimental measurement of the same variable [31].

A recent validation method is the Digital Image Correlation (DIC) [32], used to measure the full-field surface displacement of the FE model.

### 2.3.1 Digital Image Correlation (DIC)

The DIC is a cheap, easy and accurate technique suited for the study of crack propagation and material deformation. The DIC is a non-contact optical technique and provides full-field strain and displacement distribution over the specimen surface during in vitro test, instead of at a few pre-defined locations as with strain gauges. DIC works by comparing and processing digital images of the target object at different stages of deformation: by tracing sets of pixels, the DIC system can measure the surface displacement and derive full-field deformation vector field and strain map. To allow the analysis of three-dimensional deformation and the application on non-flat object, 3D DIC technique has been developed exploiting the principle of stereoscopy using two cameras. First, a reference image, which represents the object in the undeformed configuration, need to be acquired. During the mechanical test other images are captured by the cameras, at least one for each deformation condition to be investigated. These images are then compared in order to take over the displacements by searching a matched point from one image to another. It is necessary to match the same points between the images of reference and those of the deformed object. It is almost impossible to find the matched point using a single pixel because its grey level in the reference image can be found several times within subsequent images; so, the uniqueness is not guaranteed. For this reason, an area with several pixels, called subset, is used to perform the matching process. The subset has a unique grey level distribution inside itself and it is assumed that this distribution does not change during deformation. Once the location of this subset in the deformed image is found, its displacement can be determined as the shift of the central point. In order to perform this process, the surface of the object must have features that allow matching the subsets. In fact, the presence of repeated analogous subsets generates indeterminacy in the correspondence between the images and it is not possible to determine with certainty for each subset the final location as there are many possible correspondences. So, if there are not features on the surface of the object, an artificial random pattern, called speckle pattern, must be applied, for example produced by spraying paint. The speckle pattern is typically composed of dark spots of uniform size arranged on a white background to maximize the contrast. The important parameters for building a good pattern are [33]:

- The average size of the dark dots which form the pattern, that is the average diameter in pixels on the images acquired by the cameras. The optimal values range from 3 to 5 pixels.
- The coverage factor, which is the percentage of the dark pixels compared to the totally of the points acquired. Optimal measurements are ensured if it is between 40% and 70%.
- The subset entropy for the assessment of the intensity differentiation of grey levels within the same subset.

It has been shown that the characteristics of patterns directly influence the optimal subset size [33]. A cross-correlation operation is performed in order to find the correspondence between each reference subset and the corresponding portion of the image acquired during a deformed state of the body under investigation, called target subset. Once the correspondence is defined, the displacement vector is identified considering the centre of the reference target and the target subset. The figure 2.2 summarizes the principle of operation of the DIC.

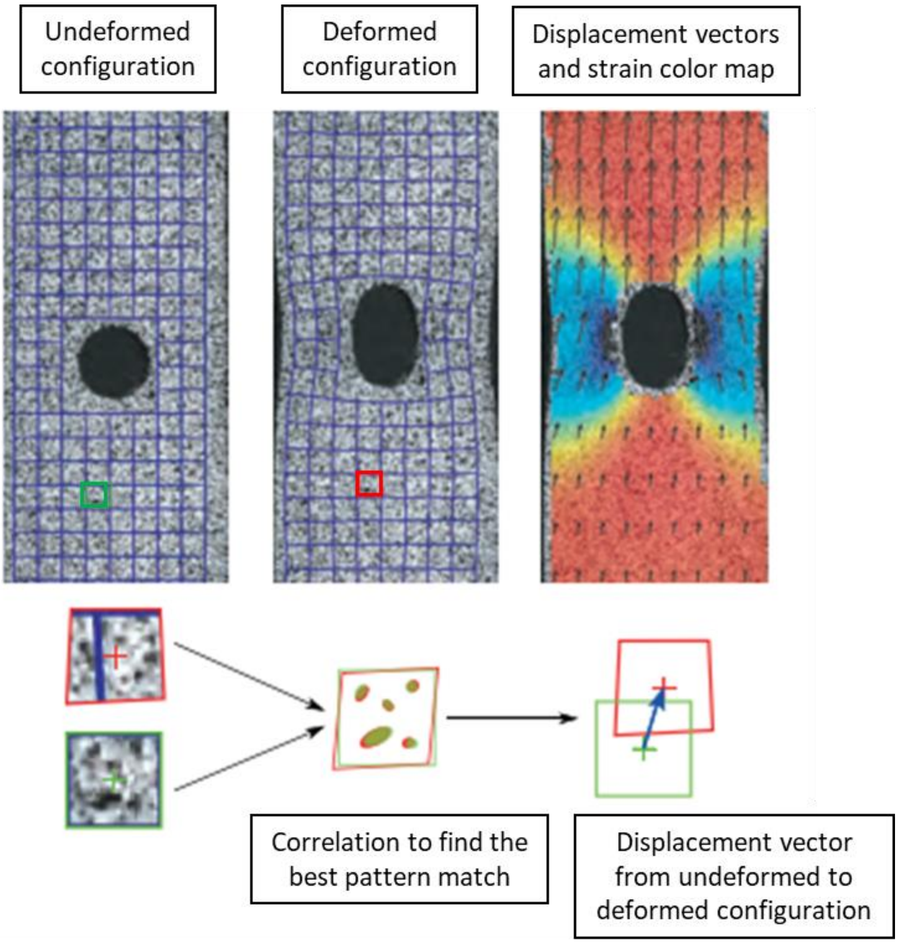

*Figure 2.2: The DIC principle of operation.*

Since DIC is not an instrument designed for the simple calculation of rigid displacements, but for more general cases in which there are fields of deformation of complexity arbitrary, it must be considered that the reference subset may not be found in the images because of the deformation. It is therefore necessary deform virtually the reference subset in order to search the best correspondence with the target subset sought. This operation to induce a deformation is carried out by shape functions, which transform the coordinates of the pixels belonging to the reference subset. Actually, the reference subset deforms independently from pixels, so the point of this subset may be in fractions of pixels, called sub-pixels, in images of the deformed configurations. For this reason, in order to obtain an accuracy sub-pixel it is necessary perform a prior interpolation operation of grey values to calculate the values also in subpixel positions. The used interpolation functions are typically polynomial or B-spline. The image matching process can return the displacement field of the analysed surface with sub-pixel resolution.

### 2.3.2 Validation of FE models of the spine with DIC method

It is possible apply the Digital Image Correlation in biomechanics to measure the full-field displacement and strain distribution on the surface of a spine segment during loading. The feasibility of using the Digital Image Correlation to quantify the full-field strain distribution on thoracolumbar spine segments was explored by Palanca et al. [34]. The results showed that the DIC, preparing adequately the specimen and setting optimal parameters, allowed to assess the strain distribution and identify the stress concentrators. The DIC, therefore, is a robust method of investigation of the spine and it can be applied in validation studies of FE models.

Gustafson et al. [18] used the DIC to validate subject-specific FE models of lumbar vertebral bodies comparing the surface displacements predicted with those experimentally measured during the mechanical test. The results showed a strong correlation between the DIC and FE displacements ($\mathrm{R}^2 = 0.75 - 0.93$), highlighting the possibility to use this metric to validate the FE models.

# 3. Development and validation of patient-specific FE models of spine segments

In this chapter the development of two patient-specific finite element models of cadaveric thoracolumbar spine segments starting from CT data will be described in detail. Later, the validation protocol, developed by the In Silico Medicine research group at the Medical Technology Lab - Rizzoli Orthopaedic Institute and at the Industrial Engineering Department - University of Bologna, will be explained and applied to the models.

## 3.1 The workflow

The main steps of the development and validation of the models were the following:

- Elaboration of the experimental data (images acquired by a QCT scan of the specimens and the displacement measurements obtained with DIC method during the mechanical tests).
- Extraction of the geometry of the specimens from the CT images in order to obtain the patient-specific models.
- Conversion of the geometries in solid models and generation of the contact surfaces between adjacent bodies.
- Tetrahedral mesh generation through the spatial discretization of the volumes in finite elements.
- Material properties assignment (intervertebral discs) and mapping (vertebrae) to mechanically characterize the models.
- Registration of DIC data on the FE models in order to compare the displacements predicted and those measured in the same coordinate reference system.
- Extraction of the translational vectors and rotation matrixes that defined the rigid body motion of the pots.
- Definition of boundary conditions (loads and constraints) to be applied in the numerical models to reproduce the experimental testing.
- FE simulations to obtain the numerical solution.
- Extraction of the nodal displacements in two Regions of Interest (ROIs) on the anterior surface of the metastatic and control vertebrae of the models.
- Comparison between the surface displacements predicted by the models with those measured experimentally using the DIC technique.

## 3.2 The experimental data

The CT scans data of the spine segments and the DIC measurements were needed to develop the FE models and validate them. In particular, the CT scans were necessary to extract the geometry of the specimens, from which it was possible generate the patient-specific models, while the DIC provided the displacements measured experimentally for the definition of the boundary conditions and the validation step.

### 3.2.1 Description of specimens

The cadaveric specimens, referred to as specimen A and specimen B, used for the development of patient-specific FE models were two human thoracolumbar segments extracted by donors with vertebral metastases derived from different primary tumours through an ethically approved donation programme (Anatomic Gifts Registry, USA). The spine segments were stored frozen so as to preserve the properties of the biological tissues and provided with all the anatomical structures (Fig 3.1).

*Figure 3.1: Frozen spine segment.*

In particular, specimen A was obtained by an 81-year-old male patient with an adrenal primary tumour, treated with chemotherapy and radiotherapy, but with no drugs. Specimen B, instead, was extracted by a 75-year-old male patient with a bladder tumour, treated only with the drug Decadron. The specimens were cleaned leaving intact the posterior ligaments and removing the anterior longitudinal ligaments and the periosteum to expose the cortical bone, which will have to be further treated for the DIC analysis. Each specimen consisted of four thoracolumbar vertebrae e three intervertebral discs (Fig 3.3). In particular, specimen A consisted of a spine segment from the T12 vertebra to L3, while specimen B from T10 to L1. The two central vertebrae of the specimens were the objects of the analysis: one, defined as “control”, was healthy (L1 and T11 respectively for specimen A and B) and one was metastatic (L2 and T12 respectively). In particular, the vertebra L2 of the specimen A had lytic type metastases and the SINS is 6, instead the metastases in the vertebra T12 in specimen B were mixed type and the SINS is 8. The configuration of these specimens allowed to study the mechanical response of control and metastatic vertebrae of two segments with the same boundary conditions during the biomechanical test. The remaining two vertebrae of the specimens, the lower and the upper ones, were embedded in polymethylmethacrylate (PMMA) to be fixed in the testing machine.

### 3.2.2 CT data description

The patient-specific models were developed starting from medical images acquired through non-destructive and non-invasive imaging techniques, such as Magnetic Resonance Imaging (MRI) or, as in this case, Computed Tomography (CT). The CT is a computerized X-ray imaging procedure and nowadays represents an essential tool in diagnostic imaging for evaluating many pathological conditions, as cerebrovascular disease, pulmonary embolism , fractures and many tumours [35]. A CT scanner includes a motorized X-ray source and a detector on opposite sides of the patient, which rotate at very high speeds around the circular opening of a structured called gantry. Each tissue absorbs the X-ray beam differently according to its composition and density and, therefore, has a different linear attenuation coefficient, $\mu$[35]. For a tissue with thickness $x$ crossed by an X-ray beam with initial and final intensity respectively $I_0$ and $I$, the attenuation coefficient can be derived from the Lambert-Beer law:

$$I = I_0 e^{-\mu x} \qquad (1)$$

The calculated attenuation coefficient $\mu$ can be normalized with respect to the attenuation coefficient of water, $\mu_{water}$, and the dimensionless value obtained from this linear transformation is expressed in Hounsfield unit (HU):

$$\mu(HU) = 1000 \cdot \frac{\mu - \mu_{water}}{\mu_{water}} \qquad (2)$$

This definition is based on the linear attenuation coefficients of water and air arbitrarily assigned in HU: the value for distilled water at standard temperature and pressure is $0\ HU$ and the value for air at standard temperature and pressure is $-1000\ HU$. The Hounsfield scale (Fig. 3.2) ranges from $-1000\ HU$ for air to a maximum of about $2000\ HU$ for very dense bones, like the cochlea, and over $3000\ HU$ for metals, like steel or silver [36].

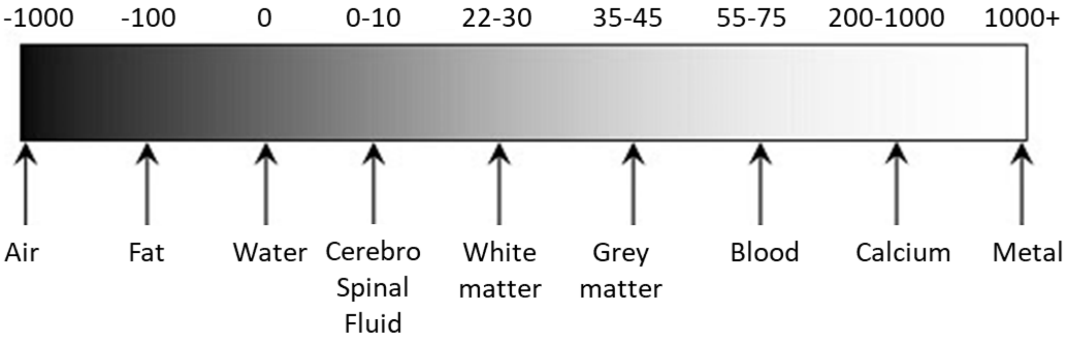

*Figure 3.2: The Hounsfield scale.*

The Hounsfield unit is a quantitative measurement of bone density, universally used in the interpretation of Computed Tomography images, where the Hounsfield scale displays as grey tones. The HU provide information of the type of the tissues and lesions: the denser tissues, which absorb more the X-ray beam, have positive values and appear bright, while the less dense tissues have negative values and appear dark. The CT images of the spine segments, mathematically reconstructed with the conventional filtered Fourier back-projection algorithm [35], represent the starting point for the development of the patient-specific models.

After the preparation of the specimens, previously described, the spine segments were analysed with the quantitative computed tomography (QCT) scanner AquilonOne (Toshiba, Japan) with a high-resolution protocol (voltage: 120 KVp, tube current: 200 mA, slice thickness: 0.5 mm, in-plane resolution: approximately 0.25 mm) (Fig. 3.3).

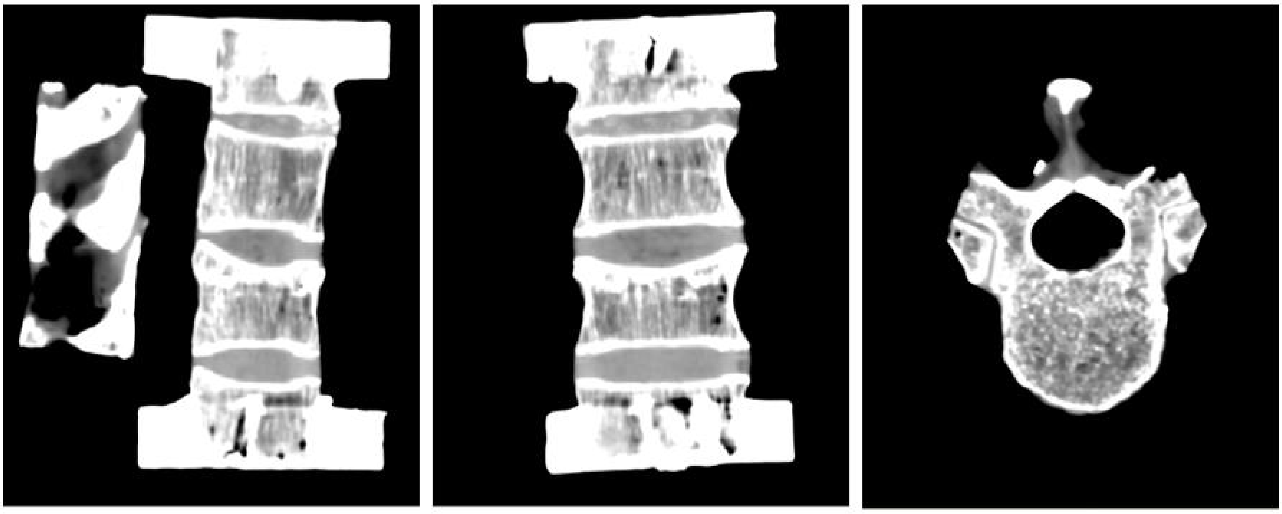

*Figure 3.3: CT images of specimen B. A: Antero-posterior view; B: Medio-lateral view; C: Superior-inferior view.*

Starting from the CT scans, it was also possible obtain the 3D reconstruction of the specimens (Fig. 3.4).

*Figure 3.4: 3D reconstruction of specimen B.*

### 3.2.3 Mechanical test and DIC data description

The specimens were subjected to a non-destructive anterior flexion test. In order to acquire the experimental measurements, the mechanical test was recorded from a DIC system (Fig. 3.5), which includes four cameras, two on each side, with different fields of view.

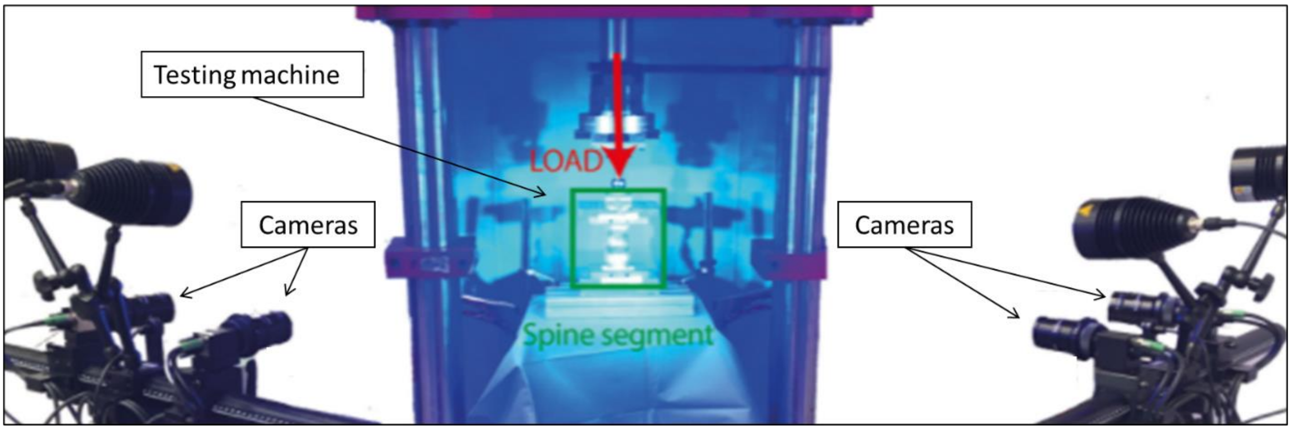

*Figure 3.5: The DIC setup.*

The mechanical test was performed using a uniaxial testing machine (Instron 8500 controller, Instron, UK), which consisted of an actuator, which applied the compressive load, two metal pots, in which the PMMA plates were placed and fixed with screw, and a load cell (Instron 25kN), which measured the vertical force (Fig. 3.6).

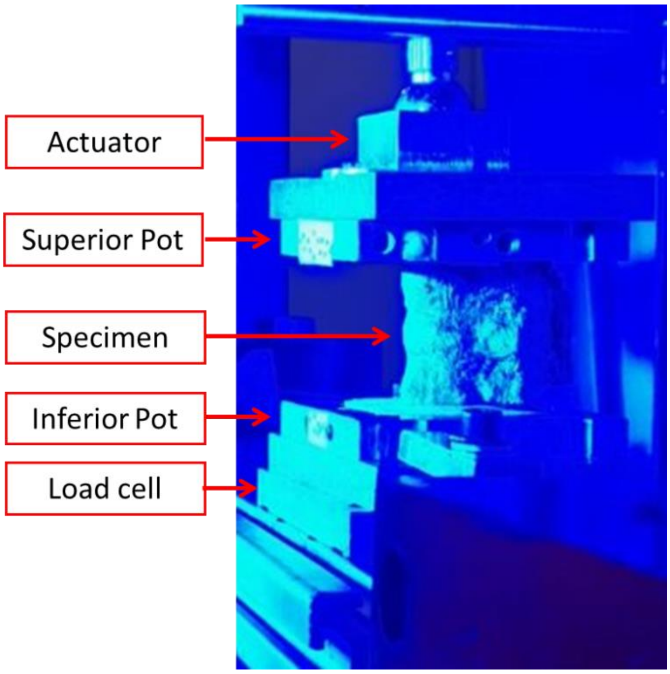

*Figure 3.6: The mechanical setup.*

Before inserting the specimens into the testing machine, their surface was prepared with a white random speckle pattern or the DIC analysis (Fig. 3.7). Furthermore, on the anterior surfaces of the pots some markers, black on white base, were positioned in order to track their displacements (Fig. 3.7).

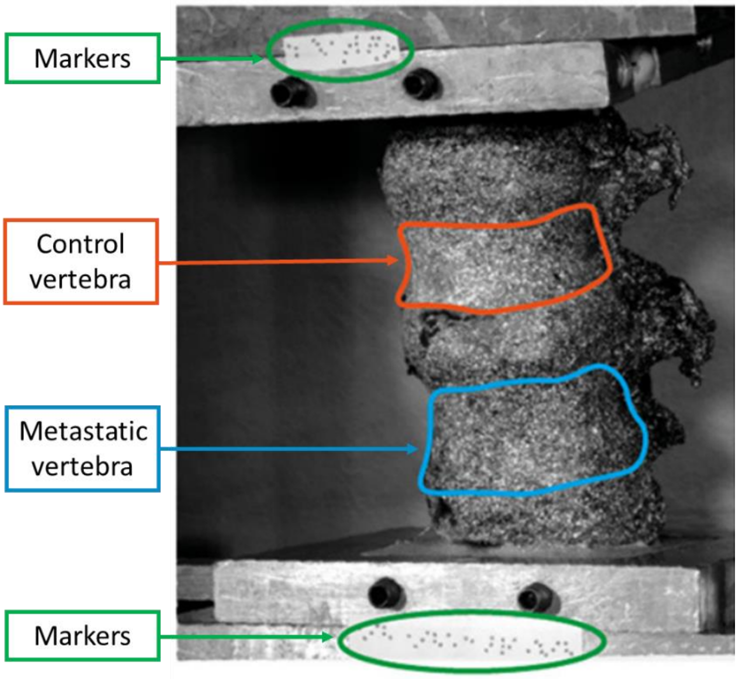

*Figure 3.7:Spine segment prepared for DIC analysis.*

During the test, the upper part of the specimens was free to translate and rotate through a ball-joint and two low-friction orthogonal linear bearing. The anterior flexion of the specimens was obtained applying a load (F) with an anterior eccentricity equal to the 10% of the antero-posterior dimension (d) of the central intervertebral disc (Fig. 3.8).

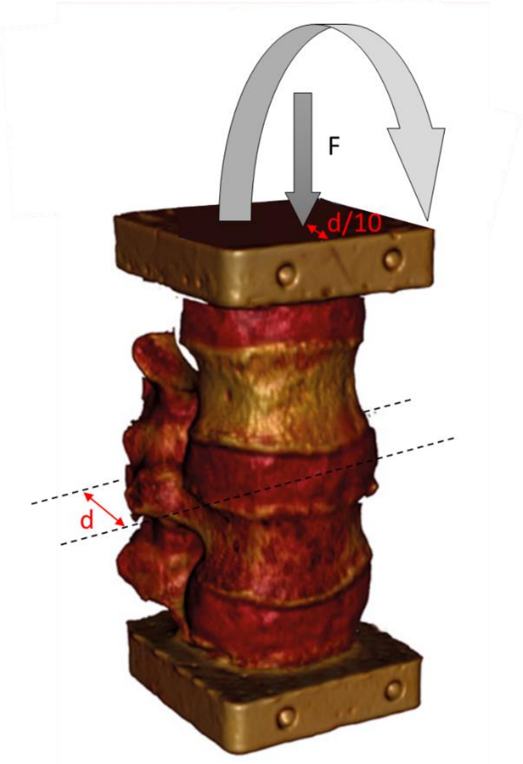

Figure 3.8: The loading conditions.

In order to achieve comparable loading conditions, the protocol tried to obtain in the control vertebral bodies of the specimens the same strain level, measured with DIC. The load was removed when the average minimum principal strain on the anterior part of the control vertebra reached about $-3000$ microstrain. This value represented the strain level measured during physiological movements, so it was chosen as a target to remain in elastic regime without causing damage to the bone. The mechanical test was thus performed: first, ten preconditioning cycles up to half to the target strain value were applied; then, the load was monotonically applied to achieve the target strain in 1 second for three load cycles. Only the second repetition was considered for the analysis of the displacements in order to avoid the initial settling of the specimens typical of the first load cycle and the eventual fractures, which could occur in the third one. During the mechanical tests the values of displacement of the actuator and the vertical force measured by the load cell were registered.

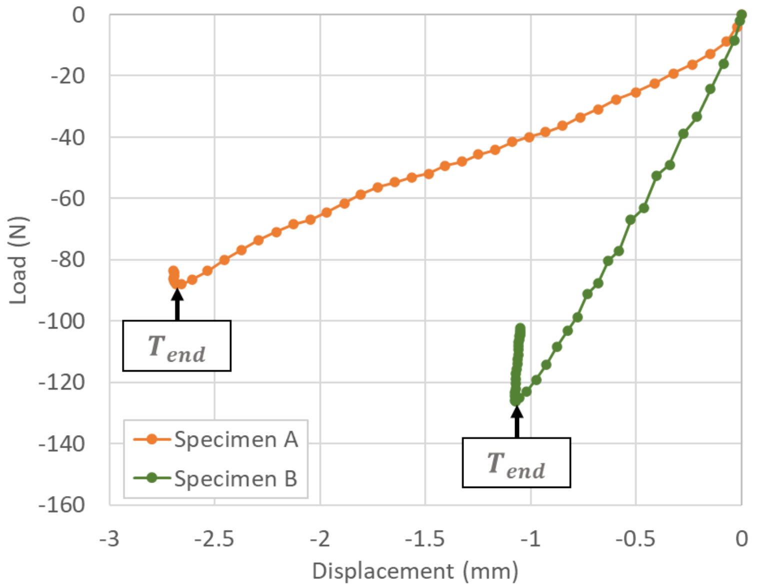

*Figure 3.9: Displacement of the actuator and vertical force during the mechanical test.*

The final loading condition considered for the FE model was defined considering the time at which the measured force reached the maximum value in absolute terms ($T_{end}$ in Fig. 3.9).

| | Load (N) | Displacement (mm) |
|---|---|---|
| **Specimen A** | -87.9622 | -2.6841 |
| **Specimen B** | -126.076 | -1.0705 |

*Table 3.1: Final values of the mechanical tests.*

A DIC system (Aramis Adjustable 12M, GOM, Germany) was used to measure the displacement and strain distributions during the tests on the anterior and lateral surface of the specimens. First, some images of the undeformed configuration of the specimens were acquired to assess the measurement uncertainties. Then, images were acquired at 25 Hz during the load. The DIC system returned a csv file for each acquisition step which contained the identification number and the values of coordinates, displacement and strain of central points of each subset of the image. The csv files were provided for both total surface of the specimens and for the single central vertebrae (L1 and L2 of specimen A, T11 and T12 of specimen B). Furthermore, csv files with the coordinates and displacements of the markers of the superior and inferior pots were also generated.

## 3.3 Generation of the model

Before performing a FEM analysis, the anatomy and morphology of the spine segments had to be reproduced, considering the geometry and the material properties. The results of the following steps were two solid models, which will be imported into a FE software.

### 3.3.1 Geometry extraction

The first step was the extraction of the geometry of the spine segments from the CT images through the segmentation, which was the process of dividing a digital image into different parts, called *Image Objects*, based on the characteristics of the pixels: a label was assigned to every pixel in the image such that pixels with the same label shared some attributes. In medical imaging the segmentation allowed to create the three-dimensional geometries of different tissues, such as bone, fibrocartilage and PMMA in this case. The segmentation method used was thresholding: the pixels of the CT images were divided comparing their HU values with a specified value (threshold). This method transformed a grey scale image in a binary image dividing it in two parts: selected and not selected sections. The nine components of the models (four vertebrae, three intervertebral discs and two pots) were segmented individually using the software 3D Slicer. First, the DICOM data, which contain the images and information about the patient and the medical examination, were imported (*Load DICOM Data*). Then, the automatic thresholding tool (*Threshold* in *Segment Editor*) in 3D Slicer, which allowed the user to set two threshold values that limit a range of HU values, was used to select the specific component to be segmented. Then, a manual segmentation, using the other commands in *Segment Editor*, was necessary in order to define the edges of geometries. The vertebrae were segmented without posterior elements because their presence was irrelevant for the study. As shown in figure 3.10, while the geometries of the vertebral bodies and the pots were extracted following their real volume profile, the intervertebral discs were segmented with a larger geometry including partially the vertebral endplates: this allowed to perform boolean operation and to create continuous contact regions between vertebrae and discs.

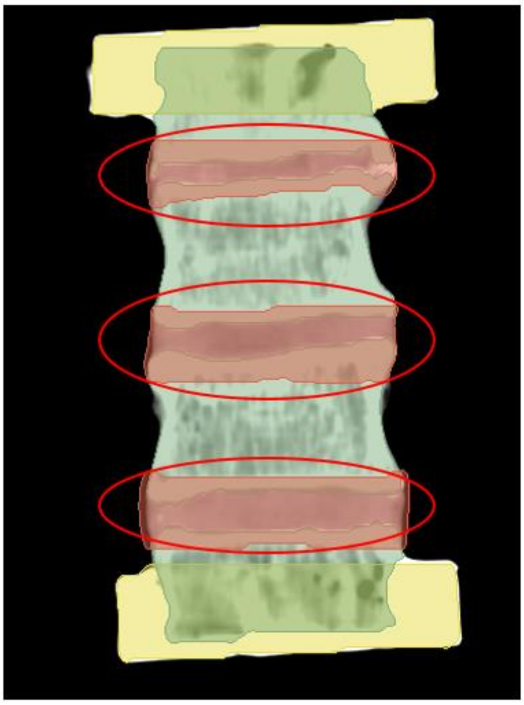

Figure 3.10: Segmentations of pots (yellow), vertebrae (green) and intervertebral disc (red).

The outputs of the segmentation step performed were STL files (Standard Tessellation Language or Standard Triangle Language), which described a triangulated surface of the three-dimensional bodies. In detail, these files contained the coordinates of the vertices (ordered by the right-hand rule) and the direction of the normal of triangles that constituted the surface using a three-dimensional Cartesian coordinate system. The units of STL files were arbitrary. The STL model, therefore, approximated the surface of a solid model with triangles (Fig. 3.11).

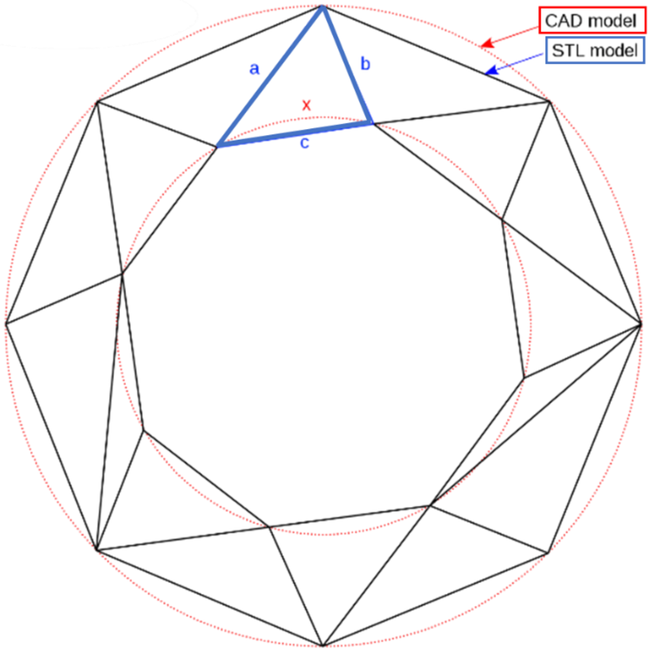

Figure 3.11: Comparison between a CAD model and the respective STL model.

The STL files were then imported in another software, ANSYS® SpaceClaim, where were considered as faceted bodies (Fig. 3.12).

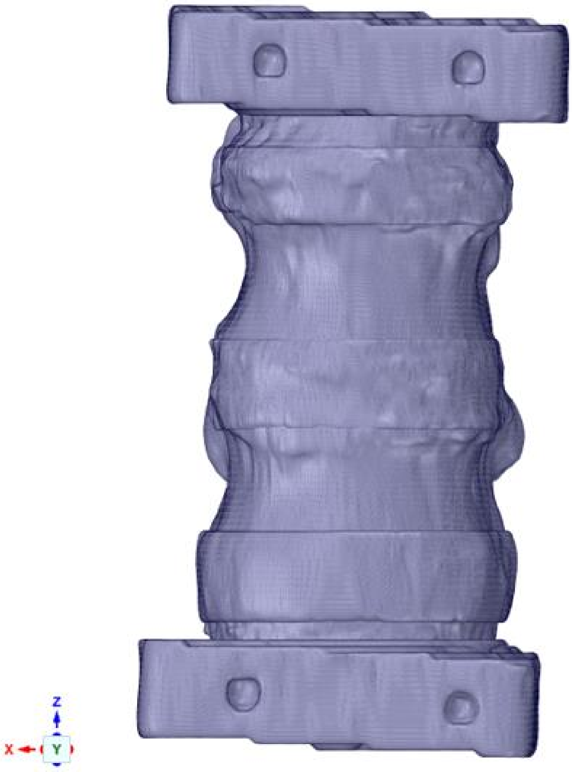

*Figure 3.12: Faceted bodies of specimen B.*

First, an automatic correction of the facets (command *Auto Fix* in *Facets*) was performed in order to fix any errors within faceted body, as openings, sharp or over-connected edges and vertices. Later, shrinkwrapped facet bodies were created (command *Shrinkwrap* in *Facets*) setting the *Gap size* equal to $0.2\,mm$. Finally, starting from faceted bodies it was possible generate solid bodies (command *Auto Skin* in *Tools*): the result of this operation was a series of patches drawn on the skin of the bodies (Fig. 3.13).

*Figure 3.13: Creation of the solid body of the vertebra T12 of specimen B.*

As previously mentioned, the complementary contact surfaces between vertebrae and intervertebral discs and between vertebrae and pots were obtained through Boolean operations, used to make combination, as merge or split, of objects. In particular, the vertebrae were subtracted from the adjacent intervertebral discs and the pots were subtracted from the extreme vertebrae (Fig. 3.14).

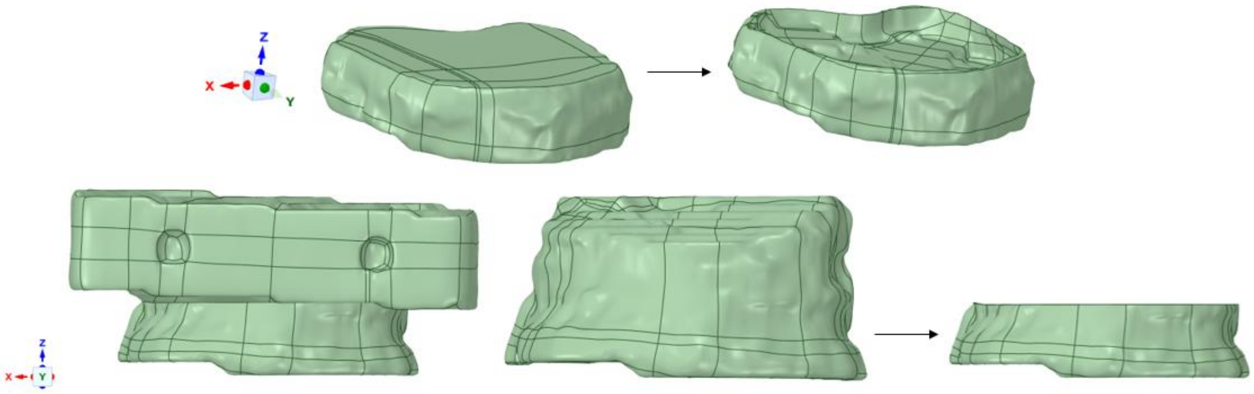

*Figure 3.14: Creation of the contact surfaces between adjacent bodies of specimen B.*

After removing the pots from the models, the STL files were finally saved and exported (Fig. 3.15).

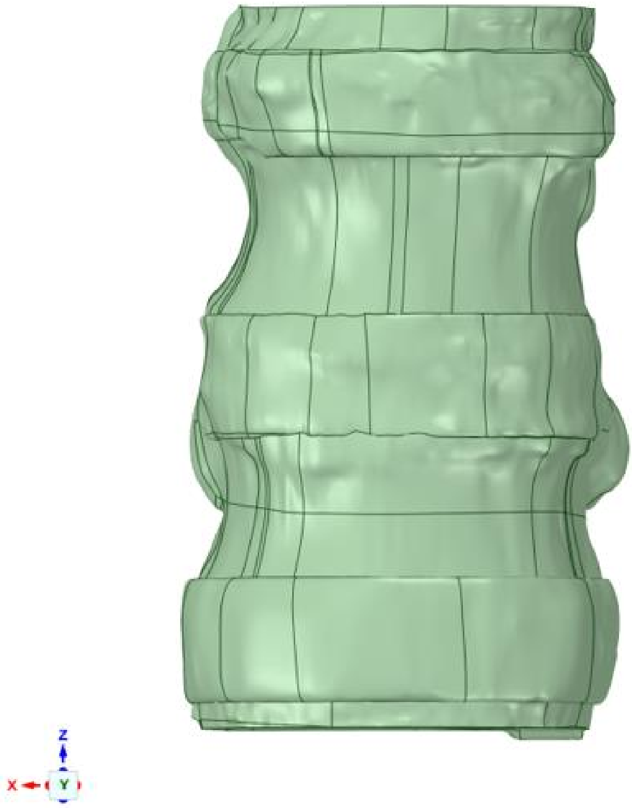

*Figure 3.15: Solid bodies of specimen B.*

### 3.3.2 Mesh generation

After generating the solid bodies, the next step was the creation of a tetra mesh, suitable for irregular geometries, such as those of bone segments obtained by CT images. The software ANSYS

ICEM CFD 2019 R3 allowed to set all parameters of interest for mesh generation in *Global Mesh Parameters* in *Global Mesh Setup* in the section *Mesh*. In particular, in *Global Element Seed Size* the *Max element* is equal to 2 $mm$; in *Shell Meshing Parameters* the *Mesh Type* is *All Tri* and the *Mesh method* is *Patch Independent; in Volume Meshing Parameter* the *Mesh Type is Tetra/Mixed; in Tetra/Mixed Meshing* the *Mesh Method* is *Robust (Octree)*. The mesh size was selected based on a convergence analysis (see section 4.2). The mesh of each body of the models was thus generated (command *Compute* in *Compute Mesh*) (Fig. 3.16).

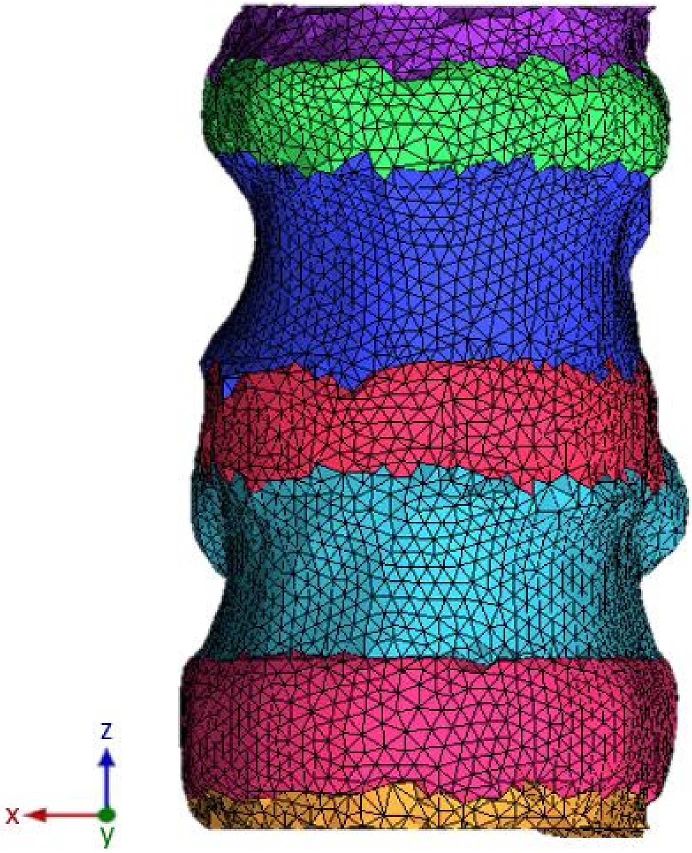

*Figure 3.16: Mesh of specimen B.*

The element initially used to discretize the models was MESH200, a tetrahedron with 4 nodes, which was a "mesh-only" element and did not contribute to the solution. This element was selected setting *Mesh-only Elements (MESH200)* as *Element Type* in *Defaults for high (*and *low) order structural 3D elements* in *Edit Parameters* in *Write/View Input File* in the *section FEA Solve Options.* The output of ICEM CFD was a .inp file, which was then imported in ANSYS Mechanical APDL 2019 R3, where all the elements MESH200 were converted in SOLID187, a tetrahedral element defined by 10 nodes

(Fig. 3.17) with three degrees of freedom at each node, well suited to modelling irregular meshes. Finally, the mesh was saved in a CDB file, an Ansys ASCII archive.

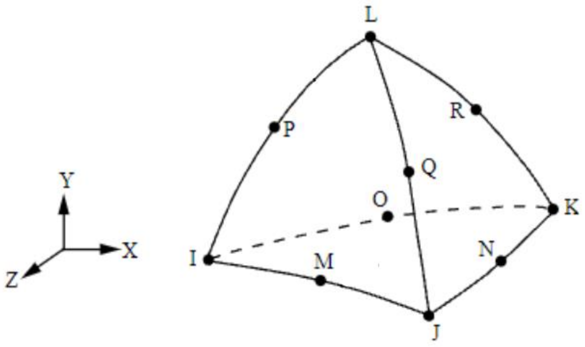

*Figure 3.17: Element SOLID187.*

### 3.3.3 Material properties assignment

The last step of the generation of the FE models was the definition of material properties in order to characterize mechanically the models. The software used to derive the heterogeneous elastic properties of the bone tissue was Bonemat, which was developed in the Rizzoli Orthopaedic Institute. Bonemat, taking the Computed Tomography images and the Finite Element model as input data, mapped on the mesh the bone elastic properties obtained from the CT image through a numerical integration algorithm [37]. The CT data, indeed, could be extensively processed to extract information both on geometry and material properties. In particular, Bonemat assigned to each element of a mesh an average material property derived from the HU values of the tissue in that region. The result was an inhomogeneous FE model, whose material properties were based on the density information contained in the CT data. To know the exact correspondence between the HU value and the Young’s modulus a densitometric calibration was necessary and it was achieved by scanning a phantom. The phantom used for spinal QCT, usually scanned before the specimen with the same acquisition parameters (generator voltage, filament current, bundle hardening filters, etc.), was the European Spine Phantom (ESP), which is currently the standard for quality control, accuracy and reproducibility measurements in spinal BMD. It had a semi-anthropomorphic shape: the main body included three vertebral inserts (L1, L2 and L3) which contained varying amounts of calcium hydroxyapatite (CaHA) to cover the full physiological range of trabecular and cortical bone densities for all age groups. The inserts were enclosed in an oval shape base of water-equivalent resin.

*Figure 3.18: European Spine Phantom.*

Bonemat used the following equations to define the bone material properties [37]:

- The CT densitometric calibration was a linear relationship which allowed to obtain a CT density value, $\rho_{QCT}$, from HU number:

  $$\rho_{QCT} = a + b \cdot HU \qquad (3)$$

  The CT density derived from CT scans of hydroxyapatite phantoms and provided information about the bone mineral content. The values of coefficients $a$ and $b$ were found through the calibration phantom and represented respectively the intercept and the slope of the regression line.

  $$\rho_{QCT} = -0.016404 + 0.00085164 \cdot HU \qquad (4)$$

- The correction of the densitometric calibration applied a linear correction to the CT calibration:

  $$\rho_{Ash} = \alpha + \beta \cdot \rho_{QCT} \qquad (5)$$

  This linear correction was necessary when evaluating bone $\rho_{Ash}$ from $\rho_{QCT}$ because the phantoms could not perfectly mimic bone characteristics. In particular, phantoms' attenuation coefficient differed from the bone due to compositional differences in the mineralised phase [38]. Furthermore, while the bone was non-homogeneous at the typical CT spatial resolution, the phantom inserts were made of a homogeneous material [38]. Not correcting the calibration could lead to underestimate $\rho_{Ash}$ for low-density tissue and overestimate $\rho_{Ash}$ for high-density tissue [38]. The relationship between $\rho_{QCT}$ and $\rho_{Ash}$ in specimens consisting of both trabecular and cortical bone had been investigated by Schileo et al. [38]. As shown in figure 3.19, the regression analysis showed an excellent correlation ($R^2 = 0.997$) and the coefficients were used to define a linear law reported in Eq. 6.

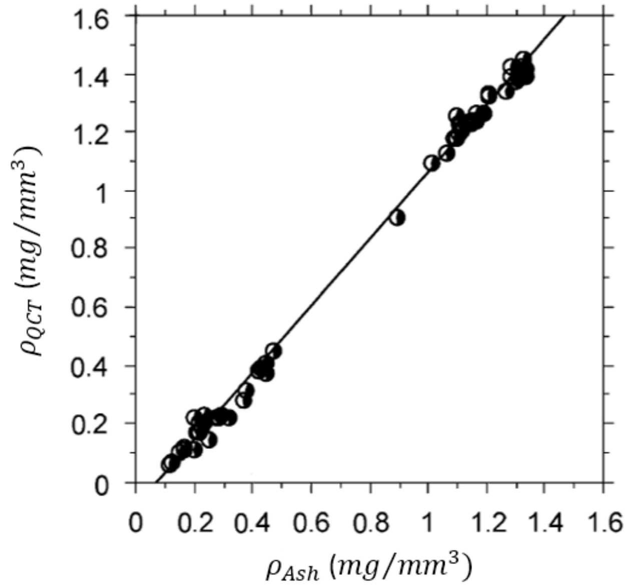

*Figure 3.19: Linear regression between $\rho_{Ash}$ and $\rho_{QCT}$ in specimens consisting of both trabecular and cortical bone [38].*

$$\rho_{Ash} = 0.079 + 0.877 \cdot \rho_{QCT} \qquad (6)$$

- The density-elasticity relationship defined the law between bone density and bone elastic modulus:

  $$E = A + B \cdot {\rho_{Ash}}^{c} \qquad (7)$$

  Indeed, once bone density information was known, the mathematical relationship with the mechanical properties remained to be established. There was no consensus about this equation, but in Bonemat reference was made to the empirical power-low relationship derived by Morgan et al. [39], which depended by the apparent density, $\rho_{App}$, that was the density measured in fresh and wet conditions:

  $$E = 4730 \cdot {\rho_{App}}^{1.56} \qquad (8)$$

  Therefore, a relationship between apparent and ash density was necessary: the $\rho_{Ash}/\rho_{App}$ ratio is assumed constant and equal to 0.6 [38]. The density-elasticity relationship becomes:

  $$E = 10494 \cdot {\rho_{Ash}}^{1.56} \qquad (9)$$

  This equation allowed to obtain the values of the elastic modulus.

The seven previous coefficients were saved in a *Configuration File*, which was imported in Bonemat along with the mesh and the CT images of each specimen. Once bone elastic properties obtained from the CT images were mapped on the mesh, a new CDB file, in which an elastic modulus value was assigned to each element, was exported.

Since Bonemat mapped the mechanical properties only on the mesh of the bone, material properties of the intervertebral discs remained to be defined. Despite the intervertebral discs are complex structures consisting of several components with different mechanical characteristics, it was assumed that they were homogeneous, linear-elastic and isotropic. Based on literature data, the Poisson's ratio was assumed equal to 0.1 [28]. Instead, in order to establish the Young's modulus of the intervertebral discs, the vertical force measured by the load cell of the testing machine was considered. In particular, after generating the models and defining the boundary conditions, a numerical simulation (described in detail in the following paragraphers) was performed in the FE software setting a generic value of Young's modulus in the physiological range. The vertical component of the reaction force predicted by the FE models was evaluated and iteratively the value of Young's modulus was changed with the aim of minimizing the difference between the force measured experimentally by the load cell during the test and the force predicted. In this way the global stiffness of the FE models was comparable to that of the specimens. At the end of this iterative process the value of Young's modulus was established for both specimens: $1.88\ MPa$ for specimen A and $6.25\ MPa$ for specimen B.

## 3.4 Registration

Once the FE models were developed, an align operation was needed in order to compare the measured and predicted displacements because the reference systems of the FE models and the corresponding DIC points were different.

The software used for the registration was Mimics Innovation Suite (MIS – Materialise NV, Leuven, BE), where the STL files of both the FE model geometries and of the DIC points in the undeformed configuration were imported and read as *Objects*. The STL files of the DIC points was provided by the DIC system for specimen B, instead the one of specimen A was created, through a triangulation algorithm implemented in Matlab, starting from the csv file that contained the coordinates of the DIC surface points in the unloaded configuration (Fig. 3.20).

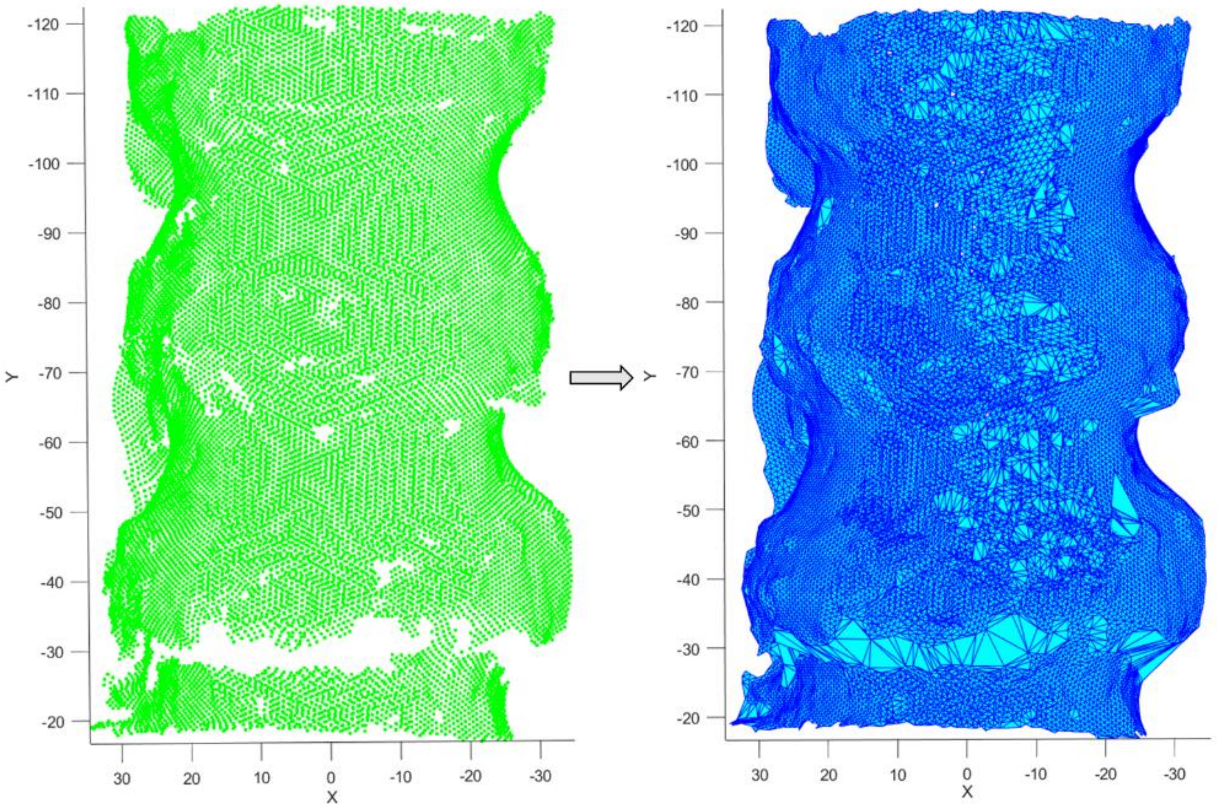

*Figure 3.20:STL (blue) generation starting from the DIC points (green) through a triangulation algorithm for specimen A.*

Before proceeding with the registration operation, it was necessary establish which was the reference STL and which was the target STL: the target was the STL of the DIC points and it was converted in masks.

First, the *Reposition* tool in *Align* section allowed to translate and rotate manually (respectively the *Translate* and the *Rotate* command) the DIC points in order to locate the STL in the neighbourhood of the mask of the model. Only when the DIC points were sufficiently close to the model surface, it was possible use the *STL Registration* function, which allowed to register an STL on a mask. Since the STL was already correctly positioned thanks to the previous operation (Fig. 3.21), the *Local Registration* algorithm was chosen because it works only on the points within a certain distance, called *Maximal distance* and set equal to 3 mm, of the edge of the mask.

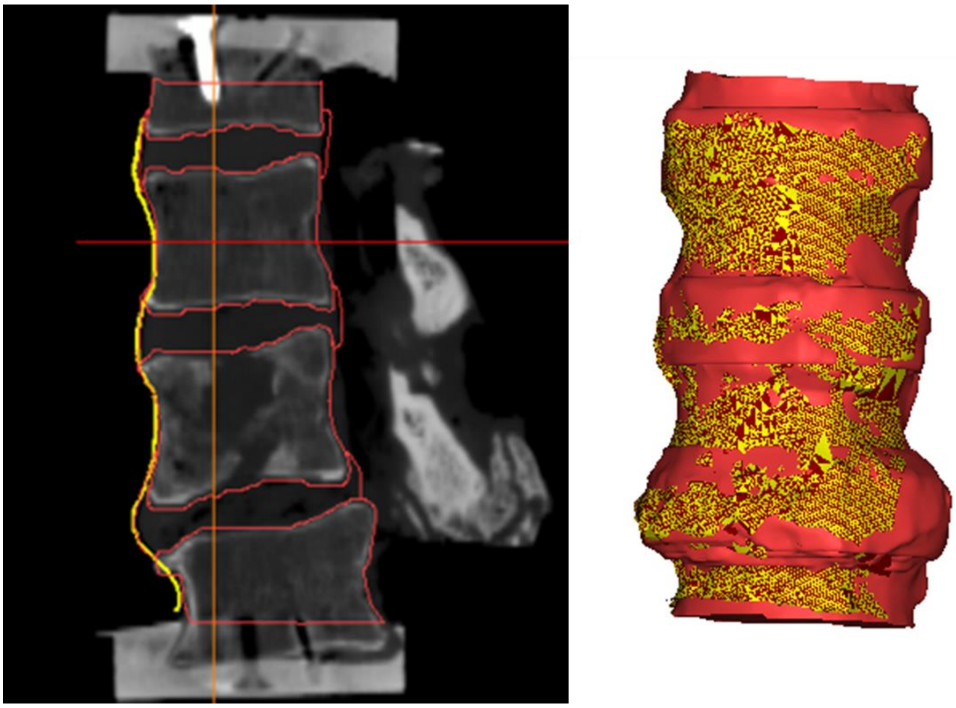

*Figure 3.211: Registration of STL (yellow) obtained by the DIC points on the FE model (red) for specimen A.*

The *STL Registration* tool also provides a value of *Least Square Distance*, which is only a qualitative error and gives an indication about the accuracy of the registration. A new STL file with the registered DIC points was exported. After the registration, it was possible compare the values of displacement predicted and measured in a common reference system defined by medio-lateral (ML), antero-posterior (AP) and superior- inferior (SI) directions.

## 3.5 Definition of the boundary conditions

After registration, the boundary conditions were defined in order to simulate the experimental testing. The software used for the following steps was Matlab.

First of all, the rigid transformation matrix $Mt$, which allowed to align the original DIC points to the registered ones, was extracted using the Singular Value Decomposition algorithm (described in detail in the section 4.1.2).

$$Mt_A = \begin{bmatrix} 0.9997 & 0.0227 & -0.0131 & 4.4397 \\ 0.0118 & 0.0549 & 0.9984 & 78.422 \\ 0.0234 & -0.9982 & 0.0547 & 1361.34 \\ 0 & 0 & 0 & 1 \end{bmatrix}$$

$$Mt_B = \begin{bmatrix} 0.9997 & 0.018 & -0.0135 & 10.09 \\ 0.0139 & -0.0215 & 0.9997 & 79.6716 \\ 0.0177 & -0.9996 & -0.0218 & 1316.07 \\ 0 & 0 & 0 & 1 \end{bmatrix}$$

The boundary conditions for the numerical simulations were extracted analysing the rigid body motion of the pots during the experimental tests. First, the coordinates of the markers placed on the anterior surfaces of the two pots in the initial and final ($T_{end}$ in Fig. 3.9) steps were transformed using the transformation matrix $Mt$. Then, as in the case of the registration of the DIC points, the Singular Value Decomposition method was used again to obtain the rotation matrices ($R_{SP}$ $and$ $R_{IP}$ ) and the translation vectors ($T_{SP}$ $and$ $T_{IP}$) that defined the rigid motion of both the superior and inferior pots.

$$R_{SP\_A} = \begin{bmatrix} 0.999 & 0.002 & -0.008 \\ -0.0007 & 0.993 & 0.114 \\ 0.008 & -0.115 & 0.993 \end{bmatrix} \quad T_{SP\_A} = \begin{bmatrix} -0.532 \\ 8.946 \\ -6.674 \end{bmatrix}$$

$$R_{IP\_A} = \begin{bmatrix} 1 & -0.000021 & -0.000005 \\ 0.00021 & 1 & -0.00005 \\ 0.000005 & -0.00005 & 1 \end{bmatrix} \quad T_{IP\_A} = \begin{bmatrix} 0.003 \\ -0.003 \\ -0.007 \end{bmatrix}$$

$$R_{SP\_B} = \begin{bmatrix} 0.999 & 0.005 & -0.002 \\ -0.005 & 0.998 & 0.049 \\ 0.002 & -0.049 & 0.998 \end{bmatrix} \quad T_{SP\_B} = \begin{bmatrix} 0.143 \\ 3.183 \\ -3.035 \end{bmatrix}$$

$$R_{IP\_B} = \begin{bmatrix} 1 & 0.000023 & -0.000053 \\ -0.000023 & 1 & 0.000035 \\ 0.000053 & -0.000035 & 1 \end{bmatrix} \quad T_{IP\_B} = \begin{bmatrix} -0.003 \\ 0.002 \\ -0.01 \end{bmatrix}$$

A conversion from rotation matrix to axis-angle convention was needed to implement the rotations in the software used for the FE simulations.

Once the rigid body motion of the pots during the experimental test was extracted, it was possible to impose the boundary conditions on the FE models. The software used for the simulation was ANSYS Mechanical APDL. The CDB file of the model was again imported and, as previously mentioned, a generic value of Young's modulus was initially set for the intervertebral discs. In order to apply the translation and rotations, a remote displacement approach was used through a Multi-Point Constraints (MPCs) algorithm that allowed to rigidly connect the nodes of the superior and inferior surface of the upper and lower vertebrae respectively to pilot nodes. Target elements were created on the pilot nodes defined on the coordinates of the centroids of the marker clusters placed on the anterior surface of the pots and extracted using the SVD, while the contact surfaces were created on the superior and inferior external nodes of the upper and lower vertebra, respectively. The rigid body motion of the pots was imposed to the pilot nodes in terms of translations and rotations (Fig. 3.22) and the finite element simulation was performed.

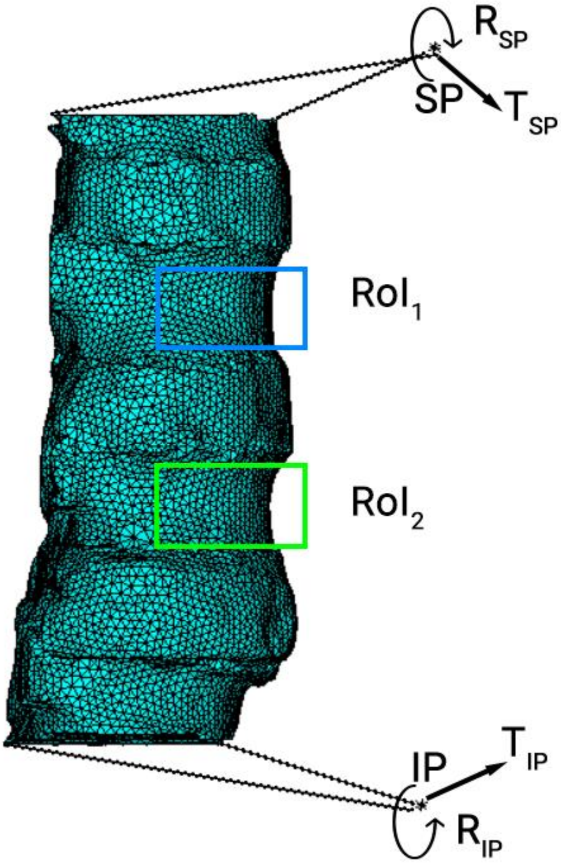

*Figure 3.22: Representation of the boundary conditions applied on the specimen A.*

When the simulation ended, the deformed configuration of the FE model was extracted (Fig. 3.23).

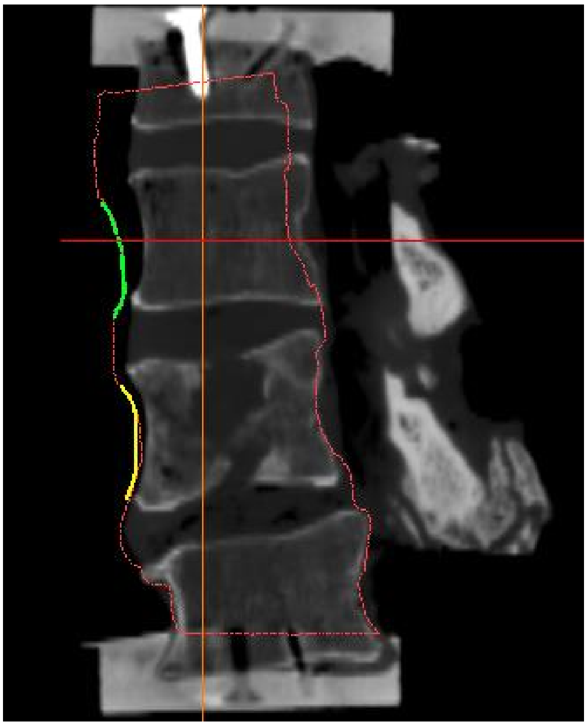

*Figure 3.223: Comparison between the deformed configuration of the FE model (red) with the transformed STL of the DIC points of the two vertebrae of the specimen A.*

## 3.6 Comparison with experimental data

The first important FE simulation result was the superior-inferior component of the reaction force extracted in the pilot node of the inferior pot. As previously anticipated, this value was inserted in an iterative process used to find the optimal value of the Young's modulus of the intervertebral discs, which allowed to obtain a global stiffness comparable to that of the experimental specimen. After establishing this value, a new simulation was run in order to obtain the displacements for the comparison with the experimental data.

To perform the comparison, two regions of interest ($RoI_1$ and $RoI_2$ in Fig. 3.22), were defined on the anterior and lateral surface of the two central vertebral bodies of each FE model. These RoIs coincided roughly with the regions captured by the DIC system during the test where the displacements were obtained. The three displacements components in the FEM nodes within the RoIs were extracted. The last operation before comparing the values of displacements was to transform the DIC data referring to the central vertebras using the matrix $Mt$ (Fig. 3.24).

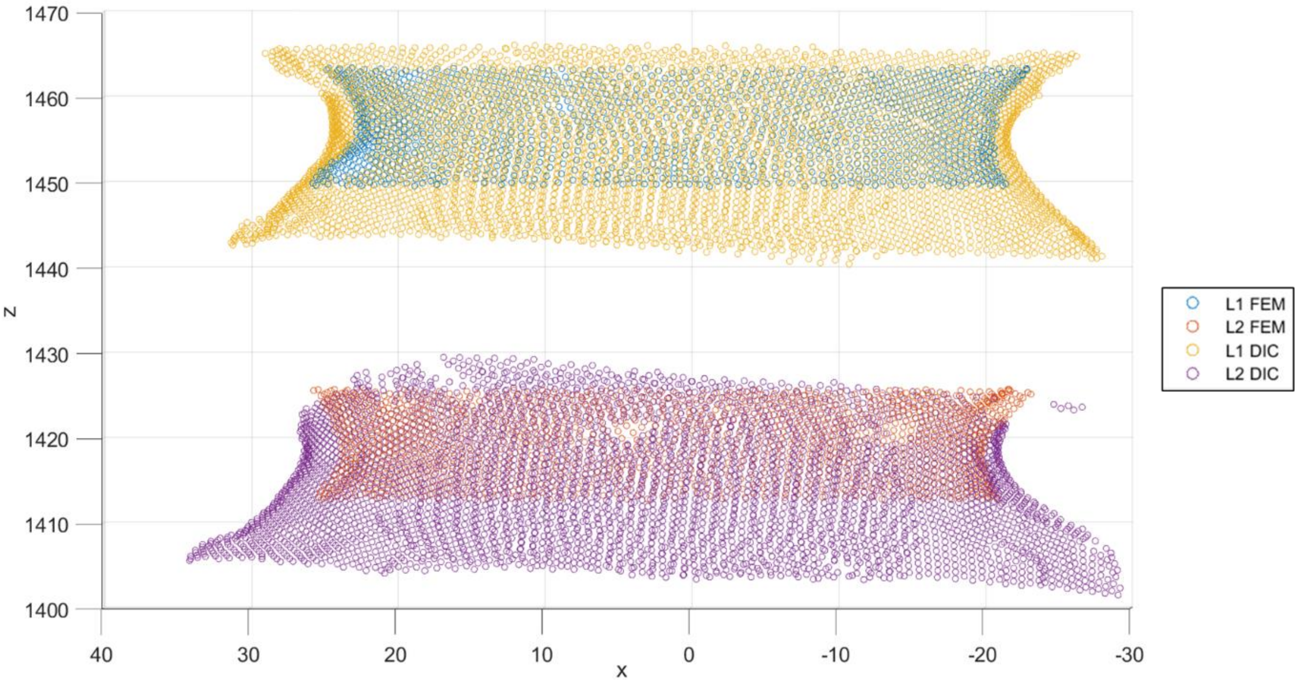

*Figure 3.24: FEM nodes of the two RoIs and DIC points of the vertebral surfaces of specimen A after the transformation.*

The DIC data were processed in order to compare them with the simulation results: the displacements were averaged on a sphere with radius R centred at the FE nodes of the RoIs. The predicted displacement in each node of the RoIs of the FE model ($U_{FEM}$) was compared point-by-point with the measured displacement averaged over the sphere centred at that node ($U_{DIC}$).

## 3.7 Results and discussion

The results of the optimization process of the Young's modulus of the intervertebral discs were first reported. Regarding the reaction force predicted by the FE models (Force FEM), only the superior-inferior component was considered because it was the only one measured (Force DIC) by the load cell of the testing machine. The percentage error $e(\%)$ was calculated as:

$$e\,\% = \frac{|Force\ FEM - Force\ DIC|}{|Force\ DIC|} \cdot 100 \qquad (10)$$

The table below shows the value of the superior-inferior component of the reaction force predicted and measured for each specimen and the corresponding percentage error.

| | **Specimen A** | **Specimen B** |
|---|---|---|
| **Force FEM (N)** | 86.794 | 126.477 |
| **Force DIC (N)** | 87.962 | 126.076 |
| **Percentage error** | 1.3 | 0.3 |

*Table 3.2: Superior-inferior component of the reaction force predicted by the models and measured experimentally and percentage error.*

The percentage error calculated for the specimen A, although higher than the one of specimen B, was still considered acceptable because less than 1.5 %.

The quality of the registration was first evaluated considering the least square distance provided by the *STL Registration* tool. Since this value represented only a qualitative estimation, some parameters were computed in order to assess quantitatively the accuracy of the registration. First, the maximum Euclidean distance between the DIC points of each vertebra and the nearest FE node in the corresponding ROI was calculated. Also, the root mean square error (RMSE) was computed. The results are reported in the table below:

| | **Specimen A** | **Specimen B** |
|---|---|---|
| **Least square distance (mm)** | 0.530 | 0.432 |
| **Maximum distance (mm)** | 0.699 | 0.9981 |
| **RMSE (mm)** | 0.08 | 0.302 |

*Table 3.3:Least square distance, maximum distance and RMSE between the DIC points and the surface of the FE models.*

The capability of the FE models to reproduce the mechanical response of the specimens under loading was evaluated with a linear regression analysis, which computes the coefficient of the line that minimizes the distance between itself and every displacement comparison points. The determination coefficient ($R^2$), which is a statistical measure of the closeness of the displacement data to the regression line, was computed. The following graphs (Fig. 3.25-3.28) show the comparison between $U_{DIC}$ and $U_{FEM}$, also reporting the regression line equations and the $R^2$ values, which quantified how close the displacement data were to the regression line. For each model, first the correlation of three displacement components is presented and then the one of the vector resultant.

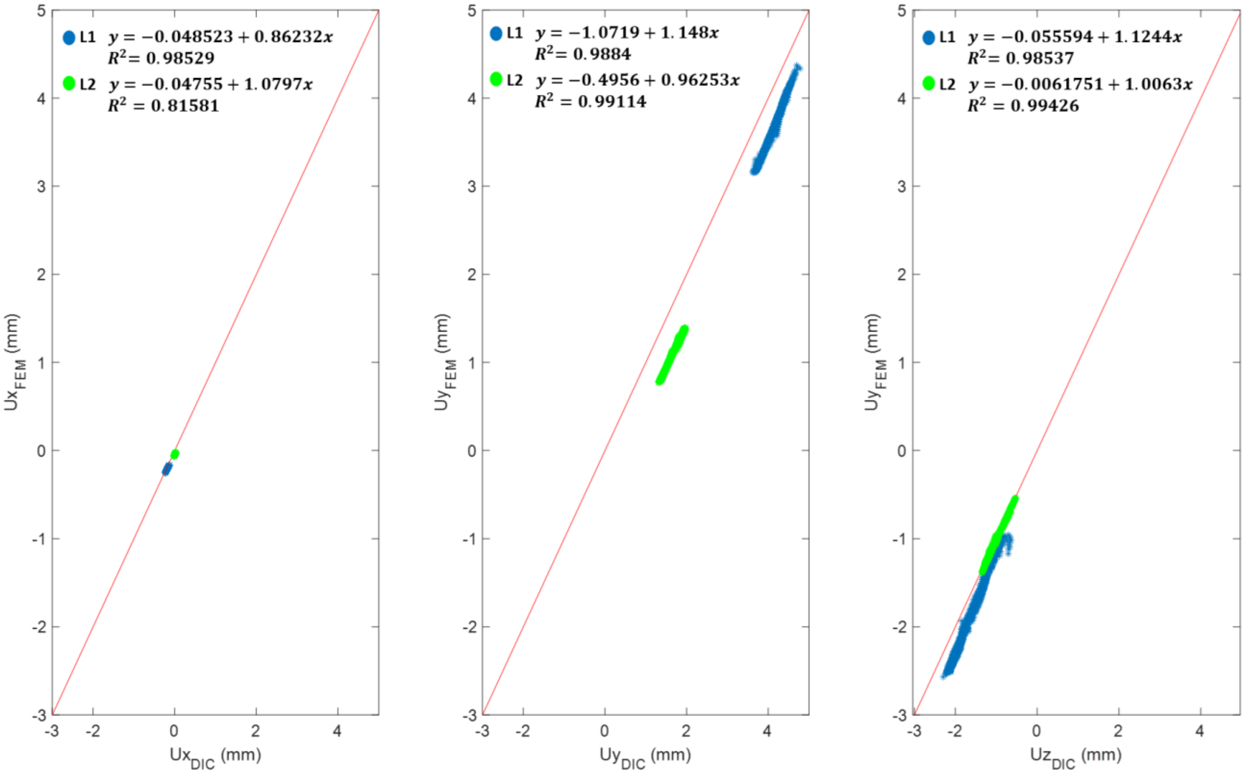

*Figure 3.25: Comparison between the displacement components measured using DIC and the ones predicted by the FE model of the specimen A for the RoIs in L1 (blue) and L2 (green) vertebrae.*

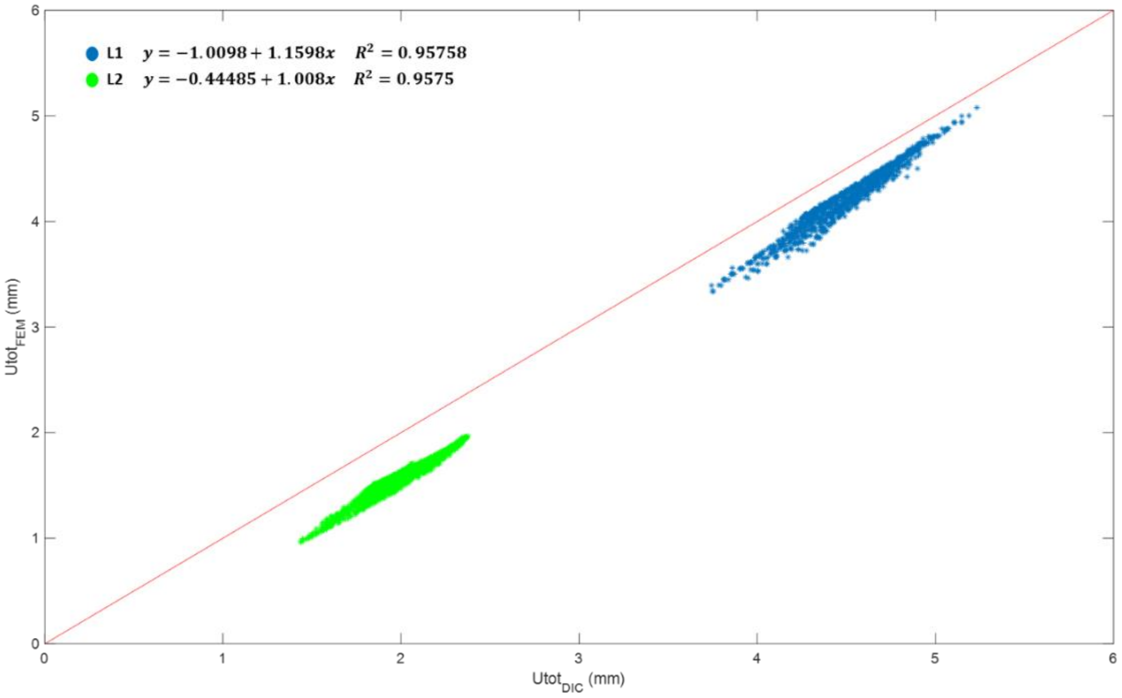

*Figure 3.26: Comparison between the displacement resultant measured using DIC and the ones predicted by the FE model of the specimen A for the RoIs in L1 (blue) and L2 (green) vertebrae.*

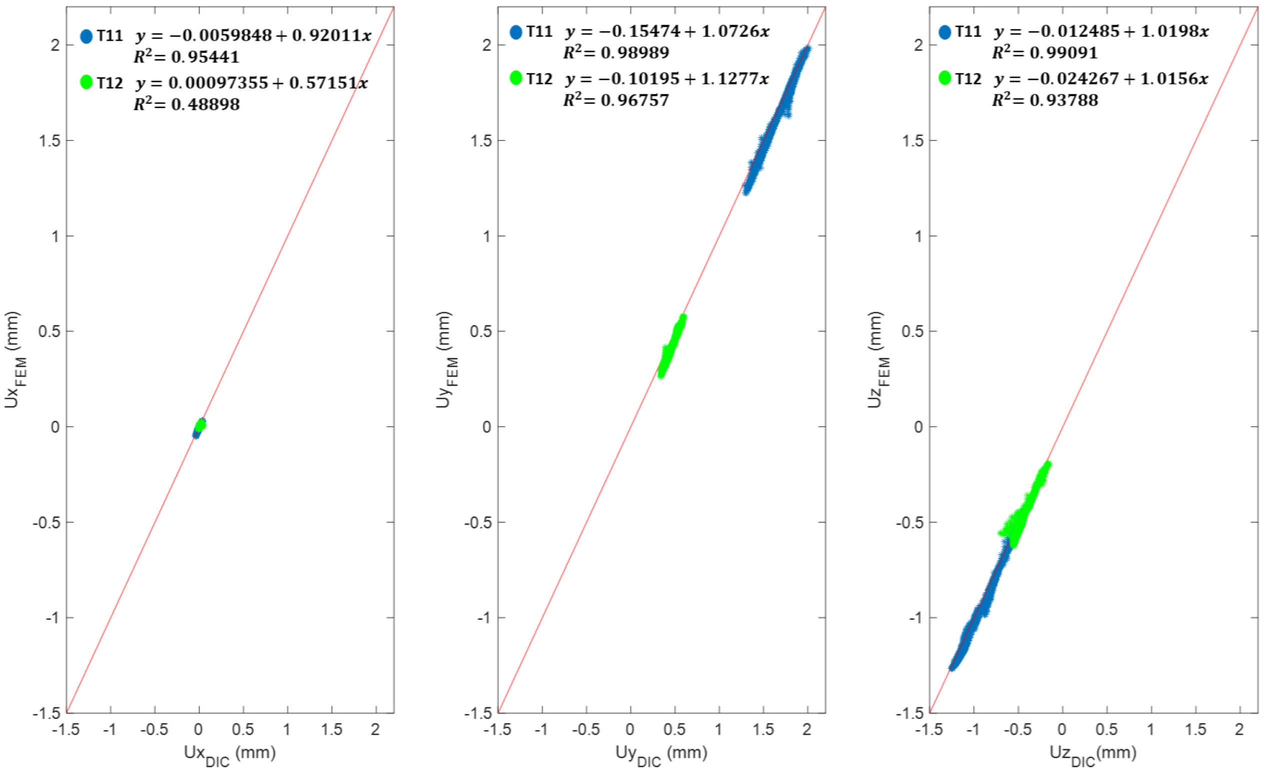

*Figure 3.27: Comparison between the displacement components measured using DIC and the ones predicted by the FE model of the specimen B for the RoIs in T11 (blue) and T12 (green) vertebrae.*

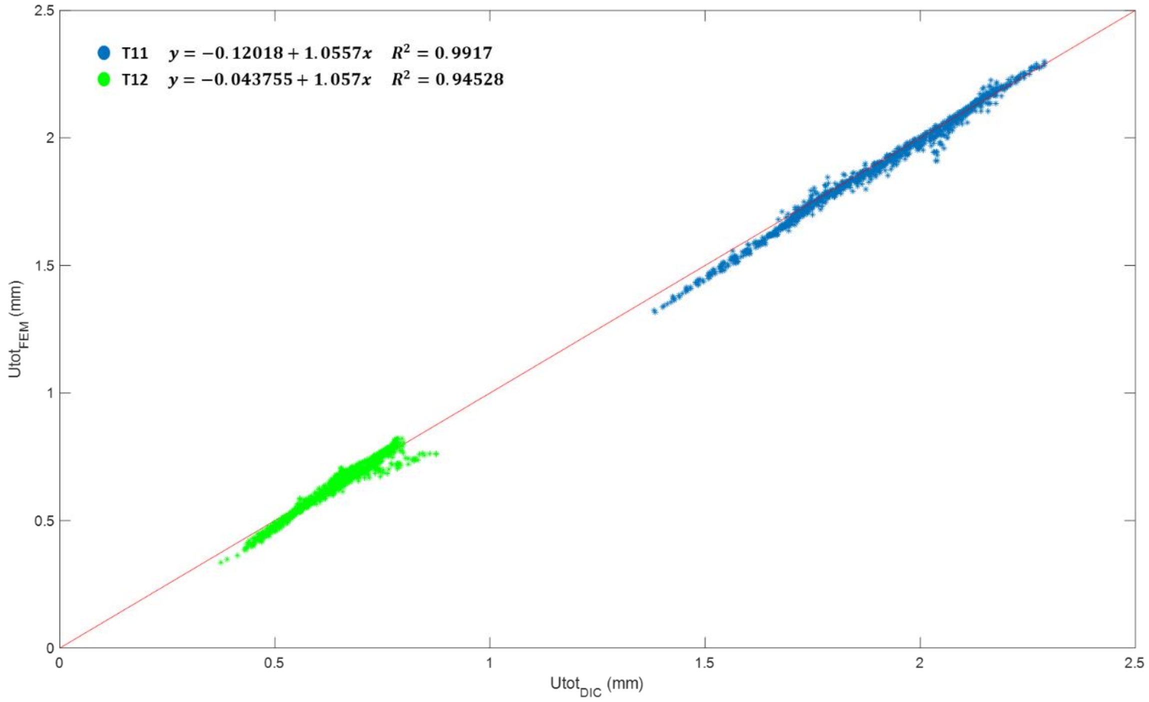

*Figure 3.28: Comparison between the displacement resultant measured using DIC and the ones predicted by the FE model of the specimen B for the RoIs in T11 (blue) and T12 (green) vertebrae.*

In addition to the determination coefficient, other variables were calculated for all directional components to assess the prediction accuracy. First, the RMSE was computed to quantify how far the predicted values were from the experimental measurement. In addition, a normalized RMSE (RMSE%) was obtained dividing the RMSE by the maximum displacement in same ROI. Then, the absolute and the percentage error were computed as follow:

$$error_{x,y,z} = \left|U_{DIC_{x,y,z}} - U_{FEM_{x,y,z}}\right| \qquad (11)$$

$$error_{x,y,z}\% = \frac{\left|U_{DIC_{x,y,z}} - U_{FEM_{x,y,z}}\right|}{\left|U_{DIC_{x,y,z}}\right|} \cdot 100 \qquad (12)$$

In each RoI the maximum absolute error (Maximum error) and the mean percentage error (Mean error %) were extracted. The table below summarizes the validation results obtained to quantify the goodness of the comparison on the three displacement components.

| | **Specimen A** | | | | | | **Specimen B** | | | | | |
|---|---|---|---|---|---|---|---|---|---|---|---|---|
| | **L1** | | | **L2** | | | **T11** | | | **T12** | | |
| | **ML** | **AP** | **SI** | **ML** | **AP** | **SI** | **ML** | **AP** | **SI** | **ML** | **AP** | **SI** |
| | **x** | **y** | **z** | **x** | **y** | **z** | **x** | **y** | **z** | **x** | **y** | **z** |
| **$R^2$** | 0.985 | 0.988 | 0.985 | 0.815 | 0.991 | 0.994 | 0.954 | 0.989 | 0.991 | 0.489 | 0.967 | 0.937 |
| **Slope** | 0.862 | 1.148 | 1.124 | 1.079 | 0.962 | 1.006 | 0.920 | 1.072 | 1.019 | 0.571 | 1.127 | 1.015 |
| **Intercept** | -0.048 | -1.072 | -0.055 | -0.047 | -0.495 | -0.006 | -0.006 | -0.154 | -0.012 | 0.001 | -0.102 | -0.024 |
| **RMSE (mm)** | 0.024 | 0.465 | 0.28 | 0.047 | 0.558 | 0.02 | 0.008 | 0.042 | 0.037 | 0.009 | 0.045 | 0.043 |
| **RMSE %** | 9.288 | 10.385 | 10.674 | 70.472 | 39.763 | 1.496 | 14.722 | 2.146 | 2.967 | 40.046 | 7.412 | 6.767 |
| **Maximum error (mm)** | 0.039 | 0.635 | 0.464 | 0.058 | 0.643 | 0.068 | 0.018 | 0.156 | 0.116 | 0.039 | 0.085 | 0.144 |
| **Mean error (mm)** | 0.024 | 0.462 | 0.271 | 0.047 | 0.557 | 0.017 | 0.007 | 0.036 | 0.032 | 0.007 | 0.042 | 0.038 |
| **Average error %** | 14.081 | 11.309 | 15.988 | 3267.463 | 34.037 | 1.640 | 347.649 | 2.337 | 3.633 | 5689.335 | 9.657 | 9.030 |

*Table 3.4: Validation results for specimen A and B.*

Finally, the vector resultant of the absolute error was computed as follow:

$$Diff = \sqrt{error_x^{\,2} + error_y^{\,2} + error_z^{\,2}} \qquad (13)$$

This quantity was also plotted (Fig. 3.29-3.30) on the FE nodes of the RoIs used for the comparison with the averaged measured displacement.

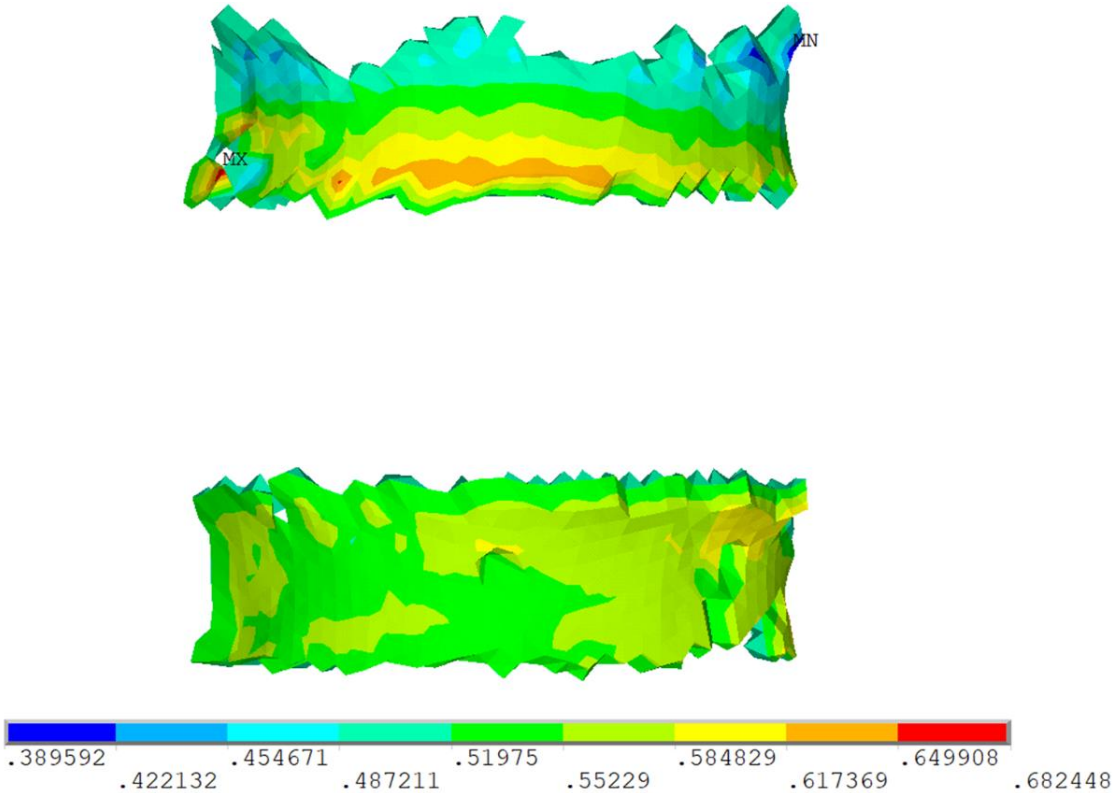

*Figure 3.29: Spatial distribution of the vector resultant (Diff) of the absolute error on the FE nodes used for the comparison of the RoIs of the FE model of the specimen A.*

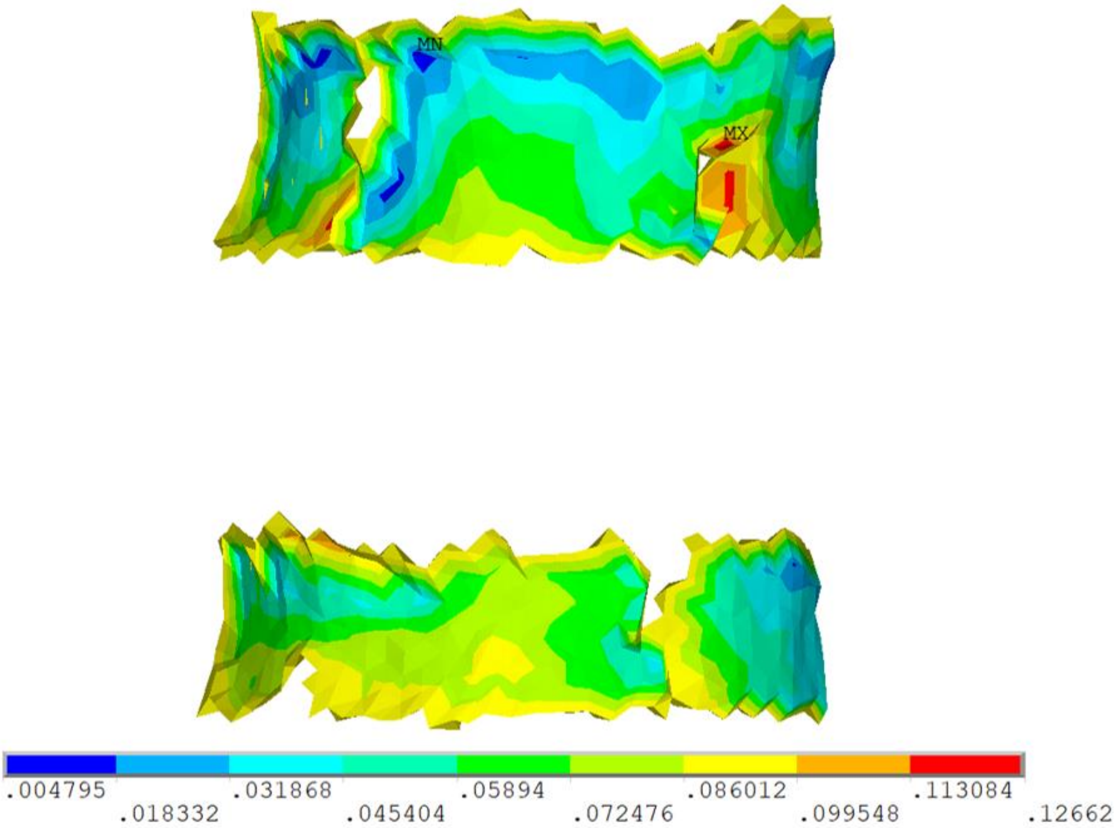

*Figure 3.30: Spatial distribution of the vector resultant (Diff) of the absolute error on the FE nodes used for the comparison of the RoIs of the FE model of the specimen B.*

The results show generally a good correlation between the displacements predicted by the FE models and the ones measured by DIC. The most critical component was the medio-lateral: in each RoI the lower values of $R^2$ and the higher RMSE % and average error % occur in this direction. On the other hand, the ML component of the displacement is smaller than the other two, so it plays a minor role in the computation of the total displacement and consequently these errors affect less the results.

The values on the AP and SI directions, in terms of RMSE % and average error %, were generally comparable, except for the L2 vertebra of the specimen A.

The maximum value of the resultant of the absolute error was found in the upper vertebra for both the FE models, which was the one with the higher displacements.

# 4. Verification studies

In order to identify and remove possible errors in the model implementation and definition of the validation protocol, some verification studies were conducted. In particular, the procedure of defining and implementing of the boundary conditions was examined in detail; the mesh convergence was analysed and, furthermore, the repeatability of the experimental measurement, on which the validation was based, was assessed.

## 4.1 The definition of the boundary conditions

The definition of the boundary conditions was a critical step of the validation protocol. The procedure of defining and implementing of the BCs was tested with a simple problem in order to verify its correctness. In detail, this analysis was performed following these steps:

- Development of an idealized FE model of spine segment.
- Simulation of the mechanical test using a full model (M1).
- Extraction of the rigid body motion of the upper pot using the Singular Value Decomposition method.
- Simulation of the same mechanical test using a reduced model (M2), where the superior metal pot was not considered and the BCs were applied trough a remote displacement-based approach.
- Comparison of the nodal displacements extracted in the region of interest between the two FE models (M1 and M2).

First, the theorical concepts needed for the understanding of the previous steps are introduced.

### 4.1.1 Multi-Point Constraints

The Multi-Point Constraints (MPCs) approach, which allows to rigidly connect different nodes coupling their degrees of freedom, is often used to apply the boundary conditions and connect rigid bodies because establishes constraint equations at the connecting surface between different elements. One application of MPCs is the use of master and slave nodes: at one independent node, called master or pilot, are connected several dependent nodes, called slaves. The displacement of the slave nodes can be forced to be the same of the pilot node. After identifying the pilot node and the slave nodes, in order to apply the MPCs in ANSYS Mechanical APDL it is necessary define two new element types: TARGE170 and CONTA174. TARGE170 element represents the target surface, on which is possible impose translation, rotation, force and moments, for the associated contact elements CONTA174. Therefore, the TARGE170 element has to be assigned to the pilot node, while the CONTA174 to the slave nodes. For both element type there are several options, called key options, which allow to define some features. In particular, for TARGE170 element, the key options were chosen as follow:

- $KEYOPT(2) = 1$ to specify the BCS for the rigid target nodes.
- $KEYOPT(4) = 111111$ to specify that all DoF (ROTZ, ROTY, ROTX, UZ, UY, UX, respectively) were constrained.

Instead, for CONTA174 element:

- $KEYOPT(2) = 2$ to select the MPCs approach as contact algorithm.
- $KEYOPT(4) = 2$ to choose a rigid surface constraint in order to constrain the contact nodes to the rigid body motion defined by the pilot node.
- $KEYOPT(12) = 5$ to select a bonded behaviour of the contact surface.

### 4.1.2 Singular Value Decomposition

The Singular Value Decomposition (SVD) is a mathematic tool which allows to compute the optimal rigid transformation that aligns two sets of corresponding points in terms of least square errors [40]. The two point sets in this case are the DIC points before, $P$, and after, $Q$, the registration.

$$P = \{p_1, p_2, p_3, \dots, p_n\}$$

$$Q = \{q_1, q_2, q_3, \dots, q_n\}$$

A rigid transformation is described by a rotation matrix $R$ and a translation vector $T$ (Fig. 4.1) such that:

$$Q = RP + T \qquad (14)$$

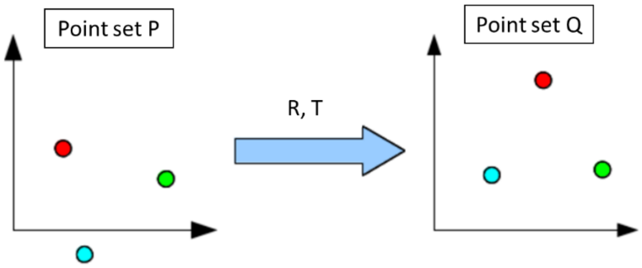

*Figure 4.1: Rigid transformation of a point set.*

The solution minimizes the least square error:

$$err = \sum_{i=1}^{n} \left\| (Rp^i + T) - q^i \right\|^2 \qquad (15)$$

First, it is necessary find the centroid of each point sets, which is the arithmetic mean position of all the points:

$$\bar{p} = \frac{\sum_{i=1}^{n} p_i}{n} \qquad (16)$$

$$\bar{q} = \frac{\sum_{i=1}^{n} q_i}{n} \qquad (17)$$

Then, the centred vectors are computed subtracting the centroid at each point in order to place both centroids of the point sets in the origin of the reference system (Fig. 4.2):

$$x_i = p_i - \bar{p} \qquad (18)$$

$$y_i = q_i - \bar{q} \qquad (19)$$

$$i = 1, 2, \ldots, n$$

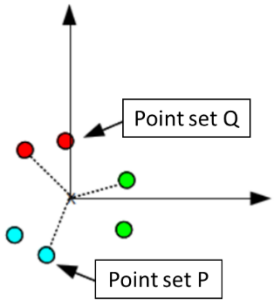

*Figure 4.2: Re-centred point sets.*

The previous operation removes the translation component and leaves only the rotation one. After collecting the vectors $x_i$ and $y_i$ as columns in two matrices, X and Y respectively, it is possible compute the covariance matrix C:

$$C = XY^T = (P - \bar{p})(Q - \bar{q})^T \qquad (20)$$

The covariance matrix can be decomposed using the SVD into three matrices: rotation (U), scaling (S) and rotation (V) matrix (Fig. 4.3).

$$C = USV^T \qquad (21)$$

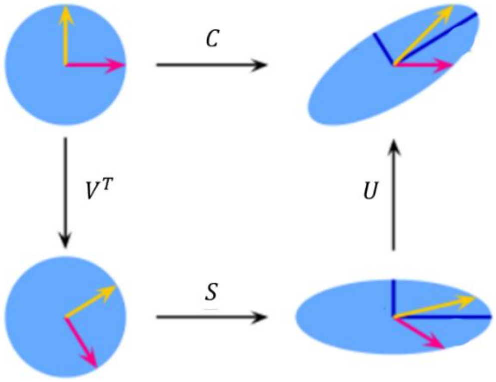

*Figure 4.3: Decomposition of the covariance matrix C into three matrices of rotation and scaling.*

In Matlab the function SVD is already implemented and allows to obtain the three matrices:

$$[U,S,V] = SVD(C) \qquad (22)$$

At this point it is possible obtain the rotation matrix $R$:

$$R = VU^T \qquad (23)$$

It is necessary to check the determinant of R because the SVD should have different correct solutions and sometimes the rotation matrix is sign reflected. If the determinant of R is negative $(-1)$, the third column of V must be multiplied by $-1$. The translation vector $T$, finally, is:

$$T = \bar{q} - R\bar{p} \qquad (24)$$

It is possible insert the rotation and the translation component in a single matrix 4x4, called transformation matrix $Mt$:

$$Mt = \begin{bmatrix} R & T \\ 0 & 1 \end{bmatrix}$$

### 4.1.3 Application of the boundary conditions

The model of spine segment, structurally similar to those developed starting from the medical images but with an idealized geometry, was created in ANSYS® SpaceClaim. The figure 4.4 shows the geometrical dimensions of the bodies:

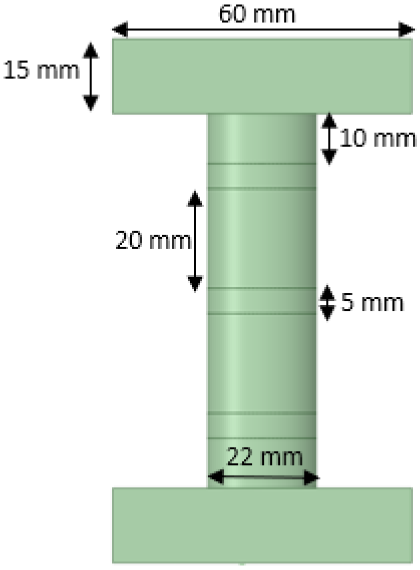

*Figure 4.4: The simplified model of spine segment.*

The mesh was generated in ICEM CFD 2019 R3 with element type SOLID187 with edge size equal to $2\ mm$. Then, the material properties were assigned based on literature [25]:

| | **Young's modulus (MPa)** | **Poisson's ratio** |
|---|---|---|
| **Intervertebral discs** | 4 | 0.4449 |
| **Vertebrae** | 2160 | 0.3 |
| **Metal pots** | 200000 | 0.3 |

*Table 4.1: Material properties.*

The anterior flexion experimental test was computationally reproduced constraining the lower surface and applying a vertical load F of 20 $N$ on the upper surface of the FE model, referred to as model 1 (M1), using the Multi-Point Constraints approach. In particular, the load was applied on the pilot node located in the anterior region of the upper surface of the superior pot, close to the centre of the square, in order to obtain the anterior flexion (Fig. 4.5).

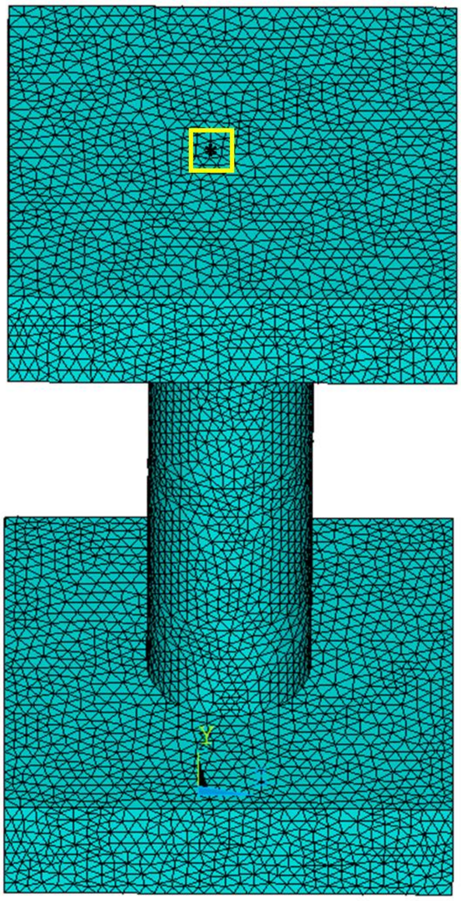

*Figure 4.5: Pilot node in the model 1.*

On the pilot node an element TARGE170 was created, while the contact elements CONTA174 were generated on the upper surface of the superior pot. Two RoIs were defined on the anterior surface of the upper vertebra (RoI$_1$) and on the anterior surface of the superior pot (RoI$_2$) (Fig. 4.6).

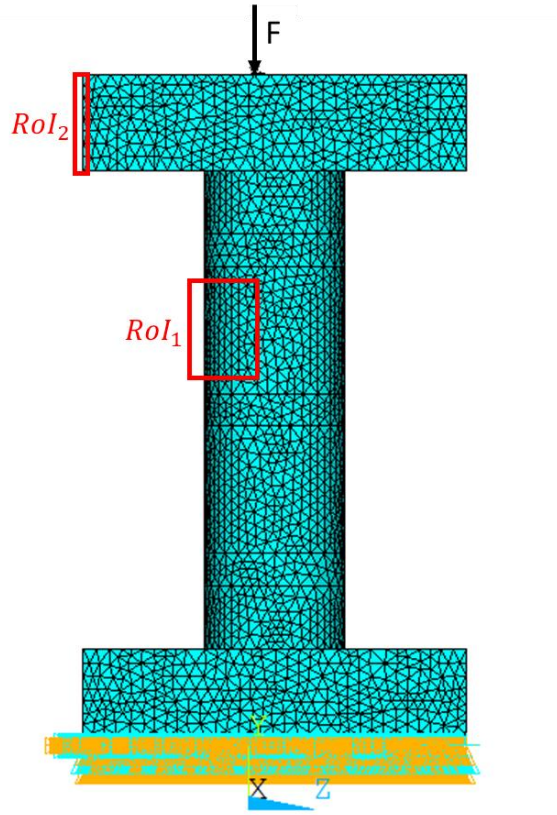

*Figure 4.6: Boundary conditions of the model 1.*

After running the FE simulation, the displacements in the $\mathrm{RoI}_1$ were saved for the comparison, while the coordinates of the nodes in $\mathrm{RoI}_2$ both in the undeformed and deformed configuration were extracted. These point sets were used to extract the rigid body motion of the superior pot during the numerical simulation, which reproduced the experimental test, through the Singular Value Decomposition algorithm. As previously described, the SVD allowed to compute the rotation matrix R and the translation vector T of the superior pot.

$$R = \begin{bmatrix} 0.999 & 0.012 & -0.0004 \\ -0.012 & 0.997 & -0.07 \\ -0.0005 & 0.07 & 0.997 \end{bmatrix} \quad T = \begin{bmatrix} -0.588 \\ -2.533 \\ -3.293 \end{bmatrix}$$

Also in this case, it was necessary a conversion from rotation matrix to axis-angle convention to implement the rotations in the software used for the FE simulations, which was ANSYS Mechanical APDL 2019 R3. These BCs were then imposed to the unloaded FE model, referred to as model 2 (M2), using again Multi-Point Constraints approach. As in the validation protocol, a target element was created on the pilot node defined on the coordinates of the centroid of the nodes in $\mathrm{RoI}_2$, while the contact surface was generated on the superior external nodes on the upper vertebra because the superior metal pot was not considered. The rigid body motion of the superior pot was imposed to the pilot node in terms of translation T and rotation R and the FE simulation was performed (Fig. 4.7).

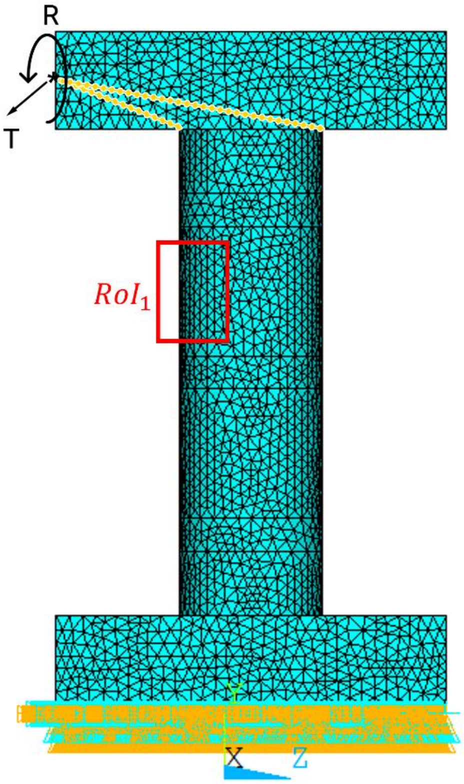

*Figure 4.7: Boundary conditions of the model 2.*

When the simulation ended, the displacements in the $\mathrm{RoI}_1$ were saved.

### 4.1.4 Results

First, the displacements in the $\mathrm{RoI}_1$ of the model 1 (Fig. 4.8) and the model 2 (Fig. 4.9) were compared.

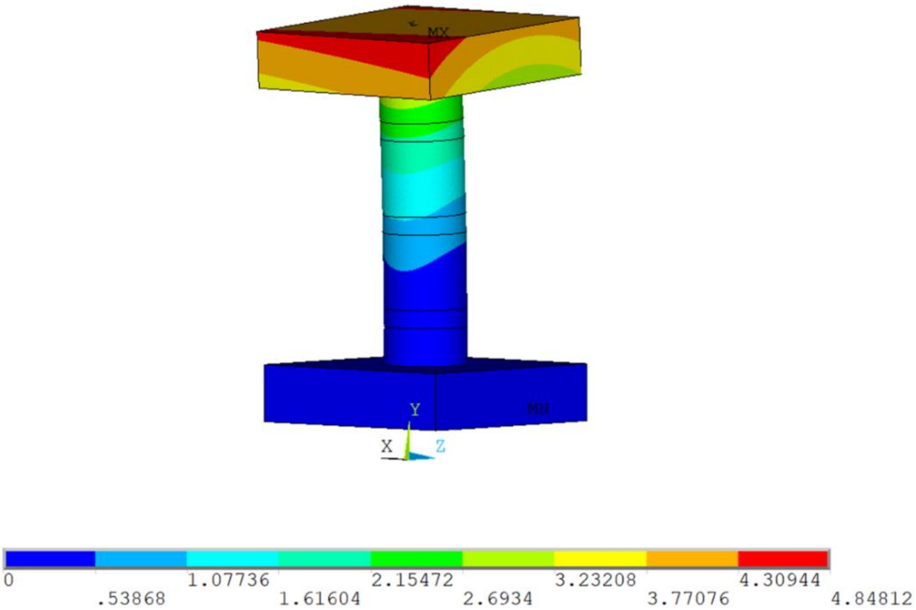

*Figure 4.8: Displacement resultant of the model 1.*

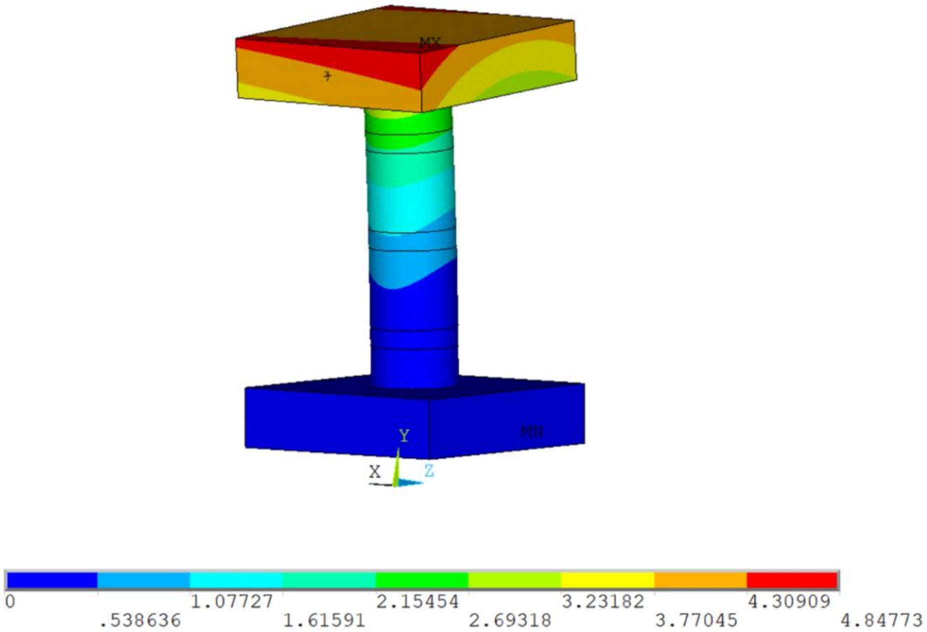

*Figure 4.9: Displacement resultant of the model 2.*

The accuracy of the definition of the BCs was evaluated with a linear regression analysis computing the determination coefficient ($R^2$). The figure 4.10 shows the comparison between the displacement components predicted in the RoI$_1$ by the model M1 ($U_{M1}$) and those predicted by the model M2 ($U_{M2}$), reporting the $R^2$ value.

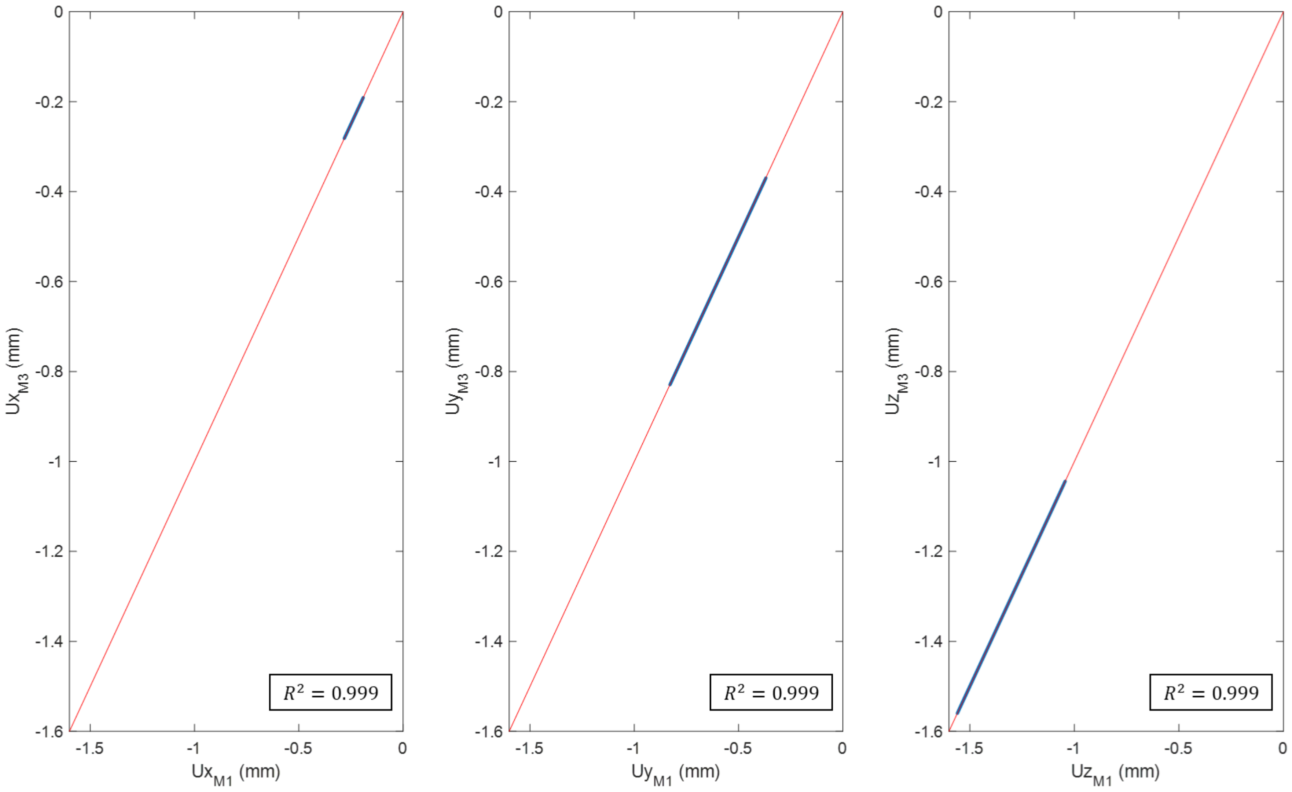

*Figure 4.10: Comparison between the displacement components predicted in the RoI$_1$ by the FE model 1 and the FE model 2.*

The $R^2$ values, close to 1, indicated an excellent correlation between the displacements predicted by the two FE models, highlighting the correctness of the procedure of defining and implementing of the boundary conditions.

In addition, a further verification was performed comparing the summation of total forces F and moments M extracted in the constrained nodes at the base of the FE models. The percentage error was computing between the reaction force of model 1 ($R_{M1}$) and model 2 ($R_{M2}$) as follow:

$$error\ \% = \frac{|R_{M2} - R_{M1}|}{|R_{M1}|} \cdot 100 \qquad (25)$$

The table below shows the values of the components of force and moment and the corresponding percentage error.

| | **M1** | **M2** | **error %** |
|---|---|---|---|
| **Fx** | 3.414e-07 | 0.0013 | 3.81e05 |
| **Fy** | -20 | -20.0382 | 0.191 |
| **Fz** | 4.97e-07 | 0.0022 | 4.43e05 |
| **Mx** | -59.6422 | -59.4084 | 0.392 |
| **My** | -3.01e-06 | 0.0463 | 1.54e06 |
| **Mz** | 64.8232 | 64.807 | 0.0251 |

*Table 4.2: Components of force and moment and the corresponding percentage error.*

As in the validation protocol, only the superior-inferior component of the force F along the y axis was considered for the comparison. The percentage error for this component of the force was among the lowest, less than 0.2 %. This result shows the similarity of the mechanical response of the two FE models.

## 4.2 Mesh convergence analysis

The FE analysis required consideration of mesh density in order to ensure adequate results from the simulations. In fact, the choice of the mesh size was a critical aspect because this parameter was closely related to the accuracy of the results. A finer mesh improved the accuracy of the analysis, but, on the other hand, a larger number of elements increased the computational time and required more computer resources [41]. A mesh convergence analysis was thus necessary to find a compromise between accuracy and efficiency. It was performed simulating the same problem with mesh elements of different size and comparing the results. As mesh density increases, the numerical results provided by the FE model should tend to a unique value.

First, a new FE model of specimen B with finer mesh was created setting $0.8\ mm$ as *Max element* in *Global Element Seed Size.* The same procedure, described in the previous chapter, was followed to assign to the model the material properties. In order to ensure the repeatability or the boundary conditions for the different models, the nodes of the RoI on the anterior surfaces of the upper vertebral bodies and of the contact surfaces were selected not manually, as in the previous analysis, but based on the spatial coordinates. The BCs were always applied using the MPCs method and a new simulation was run. The output of the simulation obtained with the fine-mesh model was considered the reference solution for the mesh convergence analysis. It was then identified the position P of the node in the RoI of the upper vertebra T12 with maximum displacements resultant. Therefore, new models with coarser meshes (*Max element* equal to $1\ mm$, $2\ mm$, $3\ mm$) were generated, ensuring that there was a node in the position P. After running the simulations for all the models, the values of the displacement of the nodes located in P, the total number of nodes and the number of the degrees of freedom (DoF) of the FE models were extracted and reported in the table below:

| | $\boldsymbol{Ux_P}$ | $\boldsymbol{Uy_P}$ | $\boldsymbol{Uz_P}$ | $\boldsymbol{Utot_P}$ | **# Nodes** | **# DoF** |
|---|---|---|---|---|---|---|
| **0.8 mm** | 0.0157 | 1.8711 | -1.2674 | 2.26 | 4131747 | 12447078 |
| **1 mm** | 0.0152 | 1.872 | -1.2641 | 2.2589 | 2147108 | 6477081 |
| **2 mm** | 0.0143 | 1.873 | -1.2578 | 2.2562 | 280075 | 848481 |
| **3 mm** | 0.0139 | 1.8685 | -1.2637 | 2.2558 | 90423 | 275697 |

*Table 4.3: Displacement values of the nodes located in P, number of nodes and number of the degrees of freedom (DoF) of the four FE models.*

The percentage difference $d_U(\%)$ between the maximum displacement in the coarser meshes ($U$) and the one in the finest mesh ($U_{Ref}$) was calculated as follow:

$$d_U(\%) = \frac{|U_{Ref} - U|}{|U_{Ref}|} \cdot 100 \qquad (26)$$

The percentage differences were calculated for the three displacements components ($d_{Ux,y,z}\%$) and the vector resultant ($d_{Utot}\%$) and were showed in the table:

| | $\boldsymbol{d_{Ux}}\%$ | $\boldsymbol{d_{Uy}}\%$ | $\boldsymbol{d_{Uz}}\%$ | $\boldsymbol{d_{Utot}}\%$ |
|---|---|---|---|---|
| **1 mm** | 3.27 | 0.048 | 0.26 | 0.0486 |
| **2 mm** | 8.72 | 0.102 | 0.757 | 0.168 |
| **3 mm** | 11.8 | 0.139 | 0.292 | 0.185 |

*Table 4.4: Percentage differences of displacement components and resultant of the three FE models.*

The change in percentage difference as a function of the number of the degrees of freedom of the FE models was plotted in figures 4.11 and 4.12.

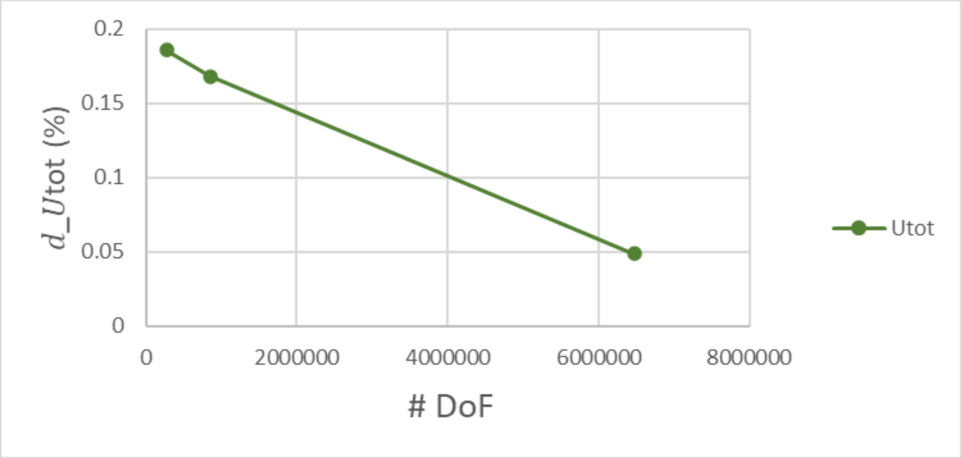

*Figure 4.11: Convergence curve of the percentage difference of displacement resultant.*

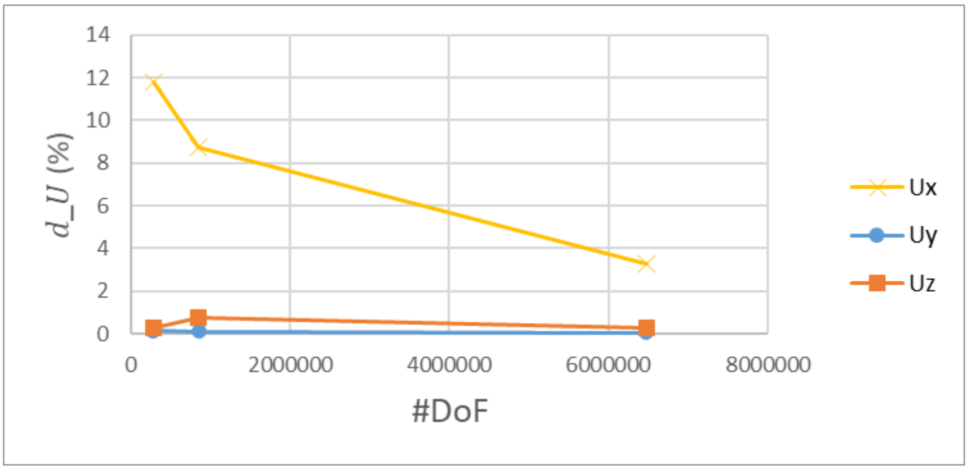

*Figure 4.12: Convergence curves of the percentage difference of displacement components.*

Despite the mesh with an element size equal to $3\ mm$ already guaranteed a negligible percentage difference in the maximum displacement (less than $0.3\%$) for the components y and z and for the vector resultant, a further mesh refinement was necessary because the values along the component x were more critical. The value of $2\ mm$ was thus chosen as mesh size to ensure a percentage difference less than $10\%$ for all the displacement components.

The mesh convergence analysis was conducted only for the FE model of the specimen B and the results were extended also to the other model.

## 4.3 Repeatability of the experimental measurements

The same experimental test described in the paragrapher 3.2.3 [17] was repeated also on another specimen, referred to as specimen C. It was obtained by a 72-year-old male patient with a nasopharyngeal primary tumour, treated only with drugs. This specimen consisted of five thoracic vertebrae, from T4 to T8. The vertebrae T5 and T6 were metastatic, while the T7 represented the control. Both vertebrae T5 and T6 presented lytic type metastases, which SINS was equal to 4.

Unlike the mechanical tests analysed in the previous chapter, in this case the values of displacement of the actuator and the vertical force measured by the load cell were recorded continuously during the three load cycles, without interrupting the recording between repetitions (Fig. 4.13). It was thus possible to use these data to assess the repeatability of the experimental measurement.

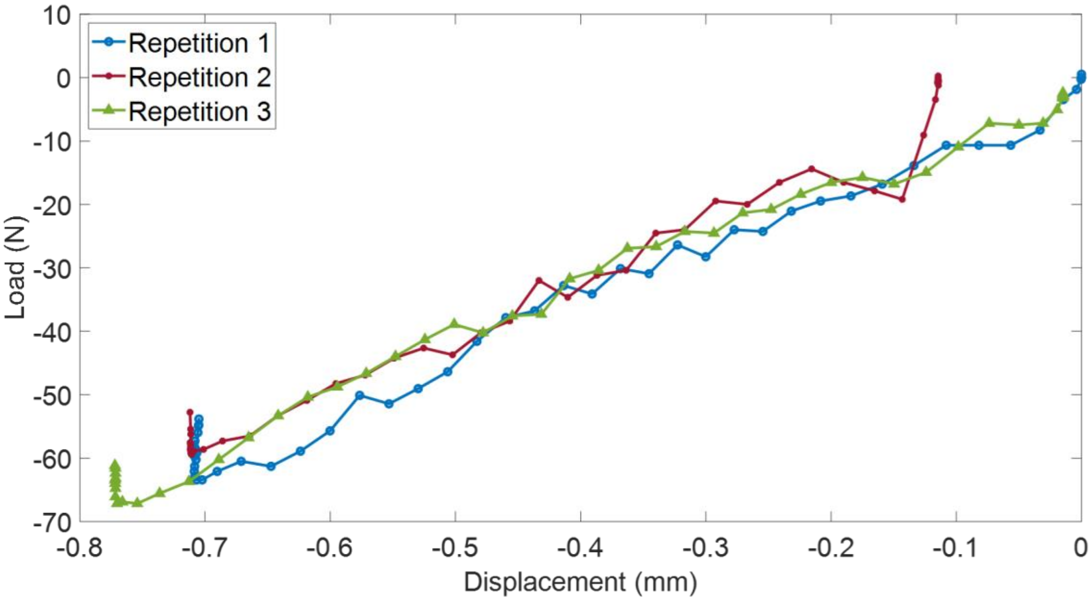

*Figure 4.13: Load-displacement curves of the three repetition during the mechanical test.*

First, these load-displacement curves were used to compute the stiffness of the specimen. Due to the different trend of the values at the start and end of each repetition, the first and last 13 frames, corresponding to the 25% of the total number of the frames, were excluded from the analysis. The values were linearly interpolated (Fig. 4.14) and the stiffness of the specimen $k$, represented by the slope of the load-displacement curves, was computed: $k = 86.34\ N/mm$ with a standard deviation of $4.2\ N/mm$.

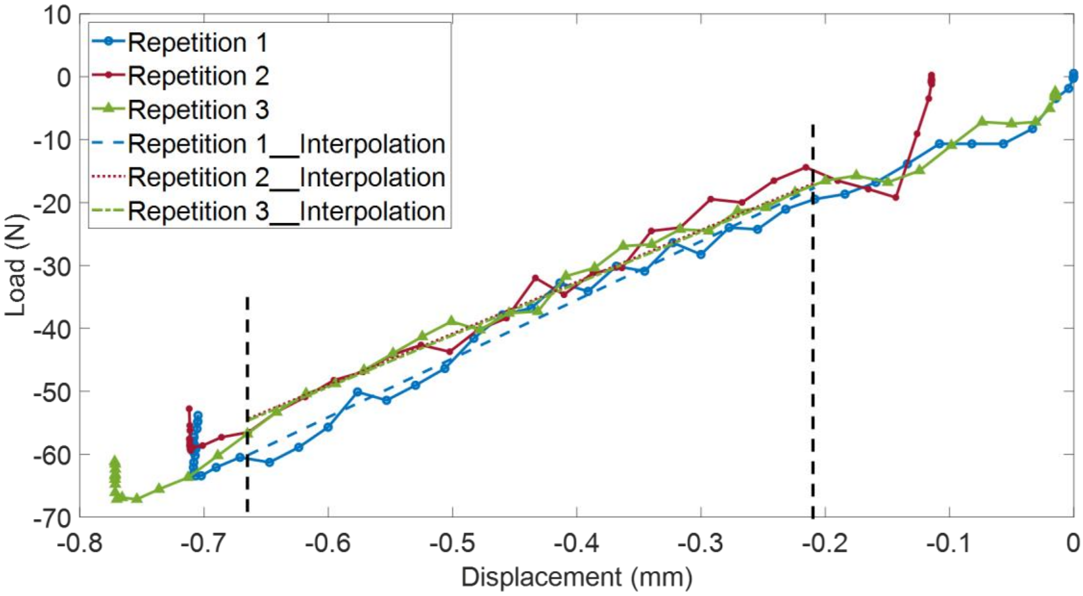

*Figure 4.14: Interpolation of the load-displacement curves of the three repetition during the mechanical test.*

Later, the repeatability of the experimental measurement was assessed. This was a crucial aspect because the validation protocol was based on the experimental data, so it was necessary to evaluate how the measurements depended on the specific repetition considered.

As previously explained, a csv file with the DIC point data (identification numbers, coordinates, displacements and strain of central points of each subset of the image) was saved for each frame recorded by the DIC system. For this analysis only the DIC points on the surface of the vertebra T5 was considered, but it was assumed that the results could be extended also to the other vertebrae. The displacement values of each DIC point were linearly interpolated. The correlation between the displacement components of the DIC points in the three repetitions (R1, R2 and R3) was analysed in correspondence of a specific load value ($F = -37.6\ N$) where the load-displacement curves were closer. Since these data were not the original experimental measurement, but were values interpolated by a line, the determination coefficient $R^2$ was equal to 1. The RMSE was also computed and reported in figure $4.15$.

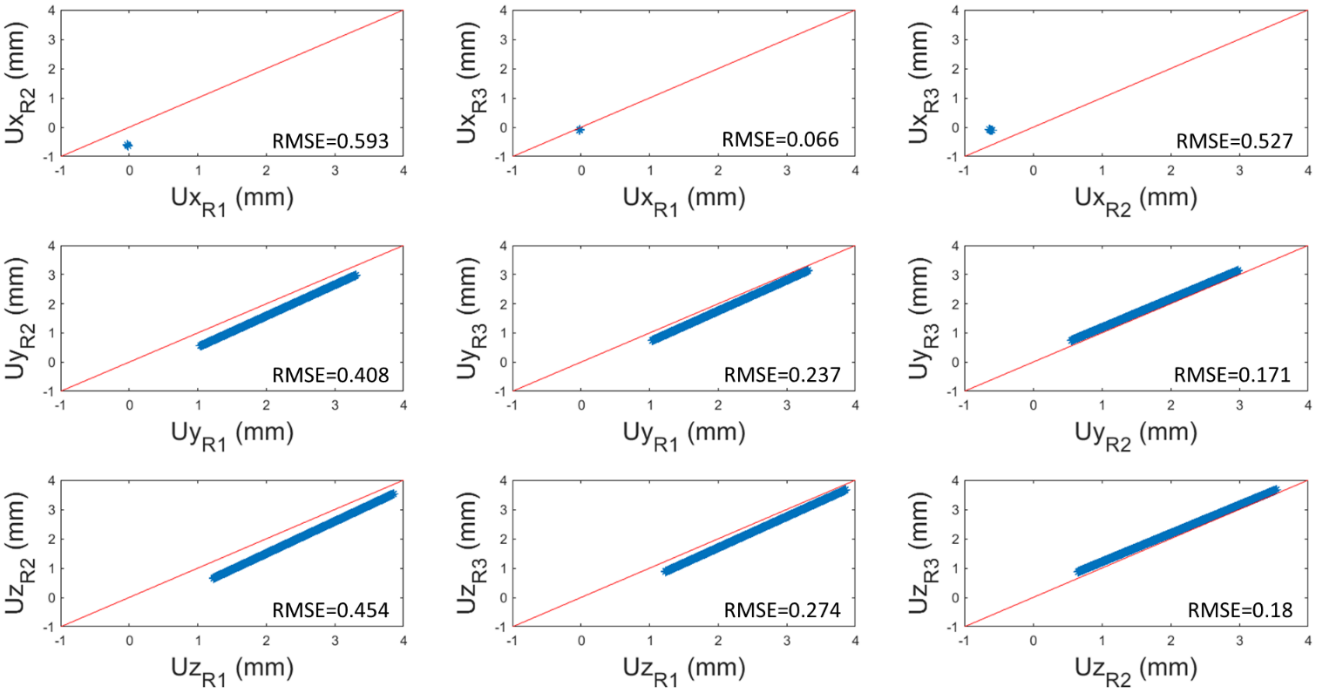

*Figure 4.15: Comparison between the displacement components measured during the three repetitions*

Considering that the displacements along the x component were less significant due to their lower order of magnitude, the repetition R2 and R3 showed the strongest correlation.

# 5. Conclusions

In conclusion, two patient-specific FE models of thoracolumbar spine segments were developed and validated using a validation protocol, recently developed by the In Silico Medicine research group at the Medical Technology Lab - Rizzoli Orthopaedic Institute and at the Industrial Engineering Department - University of Bologna. The validation was performed comparing the surface displacements of the vertebral bodies predicted by the FE models with those measured experimentally using the digital image correlation technique. Also, important verification studies were conducted to examine some critical aspects of the followed pipeline and to assess the repeatability of the experimental measurements, on which the validation is based.

The results obtained in this work demonstrated the possibility to apply the developed methodology to different case studies as it allowed to reproduce computationally the mechanical response of the cadaveric specimens under loading.

The proposed validation protocol presents several limitations.

First of all, it was applied to only two specimens, so the results cannot be easily generalised. Furthermore, the validation was based on the experimental measurements, which were affected by errors.

Finally, some strong assumptions were made to define the boundary conditions.

Also the development of the FE models presented two main critical steps: the manual segmentation to extract the geometry and the material properties assignment, which required several strong assumptions, in particular for the intervertebral discs and the metastatic vertebrae.

In addition to overcoming the previous limitations, other possible future developments could be the prediction of the bone surface strain and the assessment of the bone strength and the fracture risk in metastatic vertebrae.

# Figure index

# Table index

# Bibliography

[1] G. Anastasi *et al.*, *Anatomia umana*. Milano: Edi-Ermes.

[2] Robbins and Cotran, *Pathologic basis of disease*, Eight edition. Saunders Elsevier.

[3] E. F. Morgan, G. U. Unnikrisnan, and A. I. Hussein, 'Bone Mechanical Properties in Healthy and Diseased States', *Annu. Rev. Biomed. Eng.*, vol. 20, no. 1, pp. 119–143, Jun. 2018, doi: 10.1146/annurev-bioeng-062117-121139.

[4] *Vertebral compression fractures in osteoporotic and pathologic bone*. Springer.

[5] R. C. Schafer, *Clinical biomechanics: musculoskeletal actions and reactions*.

[6] N. Newell, J. Little, A. Christou, M. Adams, C. Adam, and S. Masouros, 'Biomechanics of the human intervertebral disc: A review of testing techniques and results', *J. Mech. Behav. Biomed. Mater.*, vol. 69, pp. 420–434, May 2017, doi: 10.1016/j.jmbbm.2017.01.037.

[7] 'A simple model for the function of proteoglycans and collagen in the response to compression of the intervertebral disc', *Proc. R. Soc. Lond. B Biol. Sci.*, vol. 249, no. 1326, pp. 281–285, Sep. 1992, doi: 10.1098/rspb.1992.0115.

[8] T. R. Oxland, 'Fundamental biomechanics of the spine—What we have learned in the past 25 years and future directions', *J. Biomech.*, vol. 49, no. 6, pp. 817–832, Apr. 2016, doi: 10.1016/j.jbiomech.2015.10.035.

[9] E. L. Radin, S. R. Simon, R. M. Rose, and I. L. Paul, *Biomeccanica in ortopedia e traumatologia*. Bologna: Aulo Gaggi Editore.

[10] A. Middleditch and J. Oliver, *Functional anatomy of the spine*. Elsevier.

[11] C.-H. Lee, P. R. Landham, R. Eastell, M. A. Adams, P. Dolan, and L. Yang, 'Development and validation of a subject-specific finite element model of the functional spinal unit to predict vertebral strength', *Proc. Inst. Mech. Eng. [H]*, vol. 231, no. 9, pp. 821–830, Sep. 2017, doi: 10.1177/0954411917708806.

[12] AIOM, AIRTUM, SIAPEC-IAP, 'I numeri del cancro in Italia nel 2020'. Intermedia editore.

[13] M. C. Costa, P. Eltes, A. Lazary, P. P. Varga, M. Viceconti, and E. Dall'Ara, 'Biomechanical assessment of vertebrae with lytic metastases with subject-specific finite element models', *J. Mech. Behav. Biomed. Mater.*, vol. 98, pp. 268–290, Oct. 2019, doi: 10.1016/j.jmbbm.2019.06.027.

[14] R. D. Ecker, T. Endo, N. M. Wetjen, and W. E. Krauss, 'Diagnosis and Treatment of Vertebral Column Metastases', *Mayo Clin. Proc.*, vol. 80, no. 9, pp. 1177–1186, Sep. 2005, doi: 10.4065/80.9.1177.

[15] M. C. Costa, L. B. B. Campello, M. Ryan, J. Rochester, M. Viceconti, and E. Dall'Ara, 'Effect of size and location of simulated lytic lesions on the structural properties of human vertebral bodies, a micro-finite element study', *Bone Rep.*, vol. 12, p. 100257, Jun. 2020, doi: 10.1016/j.bonr.2020.100257.

[16] M. A. Stadelmann *et al.*, 'Conventional finite element models estimate the strength of metastatic human vertebrae despite alterations of the bone's tissue and structure', *Bone*, vol. 141, p. 115598, Dec. 2020, doi: 10.1016/j.bone.2020.115598.

[17] M. Palanca *et al.*, 'Type, size, and position of metastatic lesions explain the deformation of the vertebrae under complex loading conditions', *Bone*, vol. 151, p. 116028, Oct. 2021, doi: 10.1016/j.bone.2021.116028.

[18] H. M. Gustafson, P. A. Cripton, S. J. Ferguson, and B. Helgason, 'Comparison of specimen-specific vertebral body finite element models with experimental digital image correlation measurements', *J. Mech. Behav. Biomed. Mater.*, vol. 65, pp. 801–807, Jan. 2017, doi: 10.1016/j.jmbbm.2016.10.002.

[19] A. A. Krishnaney, M. P. Steinmetz, and E. C. Benzel, 'Biomechanics of metastatic spine cancer', *Neurosurg. Clin. N. Am.*, vol. 15, no. 4, pp. 375–380, Oct. 2004, doi: 10.1016/j.nec.2004.04.001.

[20] M. Aebi, V. Arlet, and J. K. Webb, *Aospine manual: clinical applications*, vol. 2. Thieme.

[21] Alexander R. Vaccaro *et al.*, ‘AOSpine Thoracolumbar Spine Injury Classification System’, vol. 28, no. 23, pp. 2028–2037, 2013.

[22] Andrea Bacchetto, ‘Introduzione al metodo degli elementi finiti e alla modellazione FEM’.

[23] Enzo Tonti, ‘Introduzione elementare al metodo degli elementi finiti’.

[24] G. Guglielmi, ‘Quantitative Computed Tomography’, *Semin. Musculoskelet. Radiol.*, vol. 6, no. 3, p. 10, 2002.

[25] Zheng Wang and Haiyun Li, ‘A novel 3D finite element modeling based on medical image for intervertebral disc biomechanical analysis’, in *2005 IEEE Engineering in Medicine and Biology 27th Annual Conference*, Shanghai, China, 2005, pp. 3202–3205. doi: 10.1109/IEMBS.2005.1617157.

[26] D. H. E. Yoon, C. I. Weber, G. W. D. Easson, K. S. Broz, and S. Y. Tang, ‘Rapid determination of internal strains in soft tissues using an experimentally calibrated finite element model derived from magnetic resonance imaging’, *Quant. Imaging Med. Surg.*, vol. 10, no. 1, pp. 57–65, Jan. 2020, doi: 10.21037/qims.2019.10.16.

[27] N. Cappetti, A. Naddeo, F. Naddeo, and G. F. Solitro, ‘Finite elements/Taguchi method based procedure for the identification of the geometrical parameters significantly affecting the biomechanical behavior of a lumbar disc’, *Comput. Methods Biomech. Biomed. Engin.*, vol. 19, no. 12, pp. 1278–1285, Sep. 2016, doi: 10.1080/10255842.2015.1128529.

[28] M. Argoubi and A. Shirazi-Adl, ‘Poroelastic creep response analysis of a lumbar motion segment in compression’, *J. Biomech.*, vol. 29, no. 10, pp. 1331–1339, Oct. 1996, doi: 10.1016/0021-9290(96)00035-8.

[29] F. Gómez, R. Lorza, M. Bobadilla, and R. García, ‘Improving the Process of Adjusting the Parameters of Finite Element Models of Healthy Human Intervertebral Discs by the Multi-Response Surface Method’, *Materials*, vol. 10, no. 10, p. 1116, Sep. 2017, doi: 10.3390/ma10101116.

[30] G. Salvatore *et al.*, ‘Biomechanical effects of metastasis in the osteoporotic lumbar spine: A Finite Element Analysis’, *BMC Musculoskelet. Disord.*, vol. 19, Feb. 2018, doi: 10.1186/s12891-018-1953-6.

[31] A. C. S. Alcântara *et al.*, ‘Patient-Specific Bone Multiscale Modelling, Fracture Simulation and Risk Analysis—A Survey’, *Materials*, vol. 13, no. 1, p. 106, Dec. 2019, doi: 10.3390/ma13010106.

[32] M. C. Costa, G. Tozzi, L. Cristofolini, V. Danesi, M. Viceconti, and E. Dall’Ara, ‘Micro Finite Element models of the vertebral body: Validation of local displacement predictions’, *PLOS ONE*, vol. 12, no. 7, p. e0180151, Jul. 2017, doi: 10.1371/journal.pone.0180151.

[33] Giovanni Musotto, ‘Digital Image Correlation: applicazione di tecniche convenzionali e sviluppo di souzioni innovative per la stima e l’incremento dell’accuratezza’, Politecnico di Milano.

[34] M. Palanca, M. Marco, M. L. Ruspi, and L. Cristofolini, ‘Full-field strain distribution in multi-vertebra spine segments: An in vitro application of digital image correlation’, *Med. Eng. Phys.*, vol. 52, pp. 76–83, Feb. 2018, doi: 10.1016/j.medengphy.2017.11.003.

[35] D. T. Ginat and R. Gupta, ‘Advances in Computed Tomography Imaging Technology’, *Annu. Rev. Biomed. Eng.*, vol. 16, no. 1, pp. 431–453, Jul. 2014, doi: 10.1146/annurev-bioeng-121813-113601.

[36] Tami D. DenOtter and Johanna Schubert, ‘Hounsfield Unit’. Mar. 16, 2021.

[37] ‘Bonemat: User Guide’.

[38] E. Schileo *et al.*, ‘An accurate estimation of bone density improves the accuracy of subject-specific finite element models’, *J. Biomech.*, vol. 41, no. 11, pp. 2483–2491, Aug. 2008, doi: 10.1016/j.jbiomech.2008.05.017.

[39] E. F. Morgan, H. H. Bayraktar, and T. M. Keaveny, ‘Trabecular bone modulus–density relationships depend on anatomic site’, *J. Biomech.*, vol. 36, no. 7, pp. 897–904, Jul. 2003, doi: 10.1016/S0021-9290(03)00071-X.
[40] O. Sorkine-Hornung and M. Rabinovich, ‘Least-Squares Rigid Motion Using SVD’, p. 5.
[41] I.-T. Wang, ‘Numerical and experimental verification of finite element mesh convergence under explosion loading’. *VOLUME*, vol. 16, no. 4, p. 13.